A Reaction Mechanism for Plasma Electrolysis of $AgNO_3$ Forming Silver Nanoclusters and Nanoparticles

Astrid L. Raisanen[1], Chelsea M. Mueller[2], Subhajyoti Chaudhuri[2], George C. Schatz[2]
and Mark J. Kushner[1,3]

[1] Department of Electrical Engineering and Computer Science, University of Michigan, Ann Arbor, MI 48109-2122 USA astridr@umich.edu; mjkush@umich.edu
[2] Department of Chemistry, Northwestern University, Evanston, IL, 60208 USA chelseamueller2020@u.northwestern.edu; subhajyoti.chaudhuri@northwestern.edu; g-schatz@northwestern.edu
[3] Author to whom correspondence should be addressed

Abstract

In plasma driven solution electrolysis (PDSE), gas-phase plasma-produced species interact with an electrolytic solution to produce, for example, nanoparticles. An atmospheric pressure plasma jet (APPJ) directed onto a liquid solution containing a metallic salt will promote reduction of metallic ions in solution, generating metallic clusters which nucleate to form nanoparticles. In this article, results from a computational investigation are discussed of a PDSE process in which a radio frequency APPJ sustained in helium impinges on a silver nitrate solution, resulting in growth of silver nanoparticles. A reaction mechanism was developed and implemented in a global plasma chemistry model to predict nanoparticle growth. To develop the reaction mechanism, density functional theory (DFT) was used to generate probable silver growth pathways up to Ag_9. Neutral clusters larger than Ag_9 were classified as nanoparticles. Kinetic reaction rate coefficients for thermodynamically favorable growth pathways were estimated based on an existing, empirically determined base reaction mechanism for smaller Ag particle interactions. These rates were used in conjunction with diffusion-controlled reaction rate coefficients that were calculated for other Ag species. The role of anions in reduction of Ag_n ions in forming nanoparticles is also discussed. Oxygen containing impurities or admixtures to the helium, air entrainment into the APPJ and dissociation of saturated water vapor above the solution can produce additional reactive oxygen species (ROS) in solution, resulting in production of anions, and O_2^- in particular. For a given molarity, delivering a sufficient fluence of reducing species will produce similar nanoparticle densities and sizes for all applied power levels. Comparisons are made to alternate models for nanoparticle formation, including charged nanoparticles and use of DC plasmas.

I. Introduction

In plasma driven solution electrolysis (PDSE), gas phase plasma-liquid interactions occurring at the plasma-liquid interface perform a function that is comparable to the electron-producing metal electrode in an electrolytic cell [1]. When the plasma treats an electrolytic solution containing metallic cations, electrons and possibly anions solvating from the plasma (or produced by solvation of neutral plasma activated species) reduce the metallic cations, producing neutral metal species. The neutral species may then undergo reactions with both neutrals and cations, producing larger clusters leading to the synthesis of nanoparticles. Although the term PDSE is often associated with direct current (DC) plasma sources, the most general usage of the term PDSE would include plasmas providing reducing (or other reactive) species in place of those species originating from a solid electrode as in conventional electrolysis. As such, the term would apply to systems using any plasma source.

PDSE is often implemented using an atmospheric pressure plasma jet (APPJ) or dielectric barrier discharge (DBD) in contact with the solution. The APPJ typically consists of a rare gas, possibly with a molecular additive and with some degree of impurities, propagating into the ambient air, with its plume incident onto the surface of the solution. Progress has been made to better understand the physical, chemical, and electrical processes occurring at the plasma-liquid interfacial layer. However, the mechanisms for plasma-initiated material synthesis in the liquid phase are not well understood [2].

Silver nanoparticles have antimicrobial properties [3] and have been incorporated into materials such as nanofibers for use in applications including water filtration [4] and wound dressings [5]. To optimize PDSE for material synthesis of metals, and nanoparticles in particular, it is important to understand and control the plasma-liquid interactions that ultimately result in the reduction of metallic ions in solution. Kondeti *et al.* generated surfactant-free silver nanoparticles in solution using a radio frequency (RF) powered APPJ, noting differences in particle size distributions produced by plasmas having different gas compositions [6]. Evidence of electron-transfer at the plasma-liquid interface indicated that solvated electrons generated by the plasma were largely responsible for silver ion reduction [7]. De Vos *et. al* also suggested that solvated electrons were the main reducing species [8]. Silver and gold ion reduction rates were found to be directly proportional to the charge injected, dominantly by electrons, from a cathodic microplasma source. The resulting nanoparticles were distinct for the two metals, dependent on their individual reaction mechanisms.

It is generally accepted that reduction of Ag_n^+ by solvated electrons is a major pathway for production of nanoparticles (NP), with reduction by H atoms playing a secondary role [9]. Ghosh at al., using a dc plasma cathode in an argon gas ambient onto an $AgNO_3$ solution, measured the product Ag NPs [10]. They concluded that solvated electrons are the dominant reducing species and do so with nearly 100% Faradaic efficiency. That said, NPs are also produced under conditions where the contributions of solvated electrons are expected to be small. Shirai et al. [11] used a dual plasma electrode apparatus (plasma providing both the cathode and anode) with a $HAuCl_4$ solution and produced gold NPs at both the plasma cathode and anode interfaces, suggesting that processes in addition to reduction by solvated electrons likely occur. Patel et al. [12], employed a plasma cathode to treat a $HAuCl_4$ solution, and concluded that H_2O_2 and OH^- play major roles in gold cation reduction. Maity et al. [13] found that F^- is capable of reducing Ag ions to neutrals in aprotic solutions, whereas Cl^-, Br^- and I^- are not. Under UV illumination of silver containing organic solutions, such as humic acid, Dong et al. [14] attributed reduction of Ag^+ partially to O_2^-. On the other hand, a measurement of reaction between Ag^+ and O_2^- by Jones et al. [15] produced a rate coefficient of only 65 $M^{-1}s^{-1}$.

The shape and size of metallic nanoparticles (NPs) are dependent on the nucleation, growth, and agglomeration processes during their synthesis. Nucleation occurs when metallic ions are reduced to form seed neutral particles. Growth proceeds when seed particles combine to form clusters. Agglomeration describes the process of particle cluster aggregation. Typically, there is a competition between these three processes that describes the final nanoparticle configuration [8]. For example, smaller NPs having a higher density are formed overall if nucleation dominates over the growth. The details of the reaction mechanism and process conditions ultimately determine the size distribution of the NPs. In the synthesis of Au NPs by sonochemical reduction of $AuCl_4^-$, it was found that the size of the NPs increased, and plate formation was promoted with increasing concentration of $AuCl_4^-$. These results indicated that $AuCl_4^-$ reduction occurs preferentially on specific crystal facets of the nuclei and/or small particles [16]. In a computational study, it was found that the presence of both solvated electrons and OH radicals in a plasma-liquid system impacted the net reduction of Ag^+ in solution due to competing chemical reactions [17].

Surfactants are often used in synthesis of NPs in conventional electrolysis to stabilize the surface of growing NPs, to produce a more controlled NP size or to speed the rate of formation of

NPs. Surfactants are also used in PDSE production of NPs largely for the same reasons [6,18,19]. For example, the use of fructose, in PDSE of Ag NPs in $AgNO_3$ solutions aided in the reduction of Ag^+ by formation of aldehydes [6]. That said, the use of surfactants in PDSE appears to be less necessary to achieve monodisperse size distributions of NPs, perhaps due to the higher currents of reducing species that can be produced.

In this paper, we discuss results from a computational investigation of the synthesis of silver NPs by PDSE consisting of a helium APPJ incident onto a silver nitrate ($AgNO_3$) solution. The investigation consisted of two parts. The first was the development of a reaction mechanism describing the reduction of Ag^+ and subsequent NP nucleation, growth, and agglomeration in a water-based $AgNO_3$ solution. The second was incorporating that reaction mechanism into a global-plug-flow model of a radio frequency (RF) APPJ treating the $AgNO_3$ solution. Plasma parameters and solution properties were investigated, and their impact on the resulting NPs was evaluated.

To develop the reaction mechanism, density functional theory (DFT) was used to generate thermodynamically probable silver growth pathways up to Ag_9. Kinetic reaction rate coefficients for probable growth pathways were estimated based on a combination of existing data and theory. A semi-empirically determined base reaction mechanism was applied for smaller Ag particle interactions, and theory was applied to determine rates for exothermic reactions that occur between larger Ag particles. Neutral Ag clusters having more than nine silver atoms were grouped into a single nanoparticle species. Ostwald ripening effects were not included in this model, so the particles continued to grow with time after they were formed [20].

The combined outcome of the reaction mechanism and plasma-liquid modeling demonstrated that the path to Ag NP synthesis from water-based $AgNO_3$ solution is largely unconstrained given a large enough fluence of plasma produced reducing species, which for our conditions were dominantly solvated electrons. That said, given the large rates of production of anions in solution, small rate coefficients for reduction by anions would make a significant contribution to reduction. The unconstrained nucleation and growth process leading to NPs results from there being thermodynamically favorable pathways beginning with Ag^+ and leading to Ag_9 that provide the critical cluster size that is a precursor to NP formation. The final density and size of NPs then critically depend on the rate coefficients for agglomeration between NPs, values that were parameterized in the model. Given the thermodynamically favored pathway leading to pre-NP clusters, full reduction of Ag^+ in solution to NPs will be achieved if the fluence of reducing agents from the plasma into solution is above a critical value. The fluence of solvated electrons is clearly the major component of that critical fluence of reducing agents.

To ascertain the importance of plasma parameters on the NP synthesis, the concentration of $AgNO_3$ in solution, the composition of the plasma gases, and applied power were varied. Nucleation occurred more quickly at lower molarities, leading to larger NPs at earlier times. However, the lifetimes of clusters in solution were longer with high molarity, leading to larger nanoparticles at later times. Increasing O_2 in the APPJ gas flow resulted in larger densities of solvated reactive oxygen species (ROS). The ROS resulted in more rapid nucleation and larger NPs at early times, but smaller NPs at longer times due to competition for reducing species. Given that full reduction of Ag^+ is possible for a critical fluence of reducing species, NP size is not sensitive to APPJ power provided that the exposure produces the critical fluence.

The global plasma chemistry model used in this investigation is discussed in Section II. The silver growth pathways and reaction mechanism are discussed in Section III. The properties of the RF APPJ propagating onto a silver nitrate solution are discussed in Section IV. The evolution and dynamics of NP synthesis are discussed in Section V. Alternate models for NP synthesis are discussed in Section VI. Concluding remarks are in Section VI.

II. Description of the Global Plasma Model

The model used to investigate gas phase plasma and liquid phase solution chemistry is *GlobalKin*, a zero-dimensional (0D) plasma kinetics model operated in a plug-flow mode. *GlobalKin* addresses gas phase plasma activation of liquids by employing two zones – gas and liquid – that exchange species fluxes through the plasma-liquid interface. *GlobalKin* and its plasma-liquid algorithms have been previously described in detail and so will be only briefly discussed here [21].

Rate equations for heavy species and electrons in both the gas and liquid phases are formulated and integrated in time. For a gas phase species, *i*, the time rate of change in density, n_i, is,

$$\frac{dn_i}{dt} = \sum_j \left\{ \left(a_{ij,R} - a_{ij,L} \right) k_j \prod_l n_l^{a_{ij,L}} \right\} + \frac{1}{\tau_{flow}} \left(n_{i0} - n_i \left(1 + \frac{(P - P_0)}{P_0} \right) \right)$$
$$+ \sum_m \left\{ -\frac{D_i n_i}{\Lambda^2} f_m S_{im} + \sum_k \frac{D_k n_k}{\Lambda^2} f_m S_{km} g_{ikm} \right\} \qquad (1)$$

where $a_{ij,L}$ and $a_{ij,R}$ represent the left- and right-hand stoichiometric coefficients, respectively, of species *i* in reaction *j*. The first term on the right-hand side of Eq. (1) is the particle production rate by collisional processes by gas phase reaction *j* with reaction rate coefficient k_j that are sources or losses of species *i*. The second term represents a source for inflow and loss due to outflow, where τ_{flow} is the average residence time of the gas, n_{i0} is the density of the species flowing into the reactor, *P* is the time-dependent pressure, and P_0 is the desired operating pressure. Variation in the pressure occurs due to dissociation and gas heating. The final terms in Eq. (1) account for losses and gains due to diffusion of species to *m* unique surfaces having fractional area f_m. Reactions on the surfaces consume and generate species. D_i is the diffusion coefficient, and Λ is the diffusion length. A fraction S_{im} of species *i* react on surface *m* and are lost from the gas phase. The first sum accounts for losses of species i on surfaces. The second sum accounts for production of species *i* on surface by reactions of species *k* with a branching ratio to species i of g_{ikm}.

For this study, *GlobalKin* was employed in a plug flow mode through a cylindrical tube. In plug flow, a volume of gas is followed as it translates from the gas inlet to the liquid surface while accounting for diffusion processes in the radial direction. The initial axial speed is given by the inlet flow rate, pressure, and diameter of the tube. Assuming isobaric conditions, the time rate of change of the axial speed is given by

$$\frac{dv}{dt} = \frac{v}{\tau_f}\frac{(P-P_0)}{P_0} \tag{2}$$

where τ_f is the time required for pressure waves to cross the flow tube.

The gas temperature, T_g, is produced by

$$\begin{aligned}\frac{\partial\left(N_g c_p T_g\right)}{\partial t} &= P_{ion} + \sum_i \frac{3}{2} n_e N_i k_{mi}\left(\frac{2m_e}{M_i}\right) k_B\left(T_e - T_i\right) + \sum_i \Delta\varepsilon_i R_i - \sum_i \Delta H_i R_i \\ &\quad + \frac{1}{\tau_{flow}}\left(N_{g0} c_{p0} T_{g0} - N_g c_p T_g\right) - \frac{\kappa}{\Lambda^2}\left(T_g - T_w\right)\end{aligned} \tag{3}$$

where N_g is the total gas density, c_p is the specific heat of the gas at constant pressure, m_e is the electron mass, M_i is the particle mass of species *i*, k_B is Boltzmann's constant, and T_e is the electron temperature. P_{ion} is the power deposited into ions by the ambipolar electric fields. The second term on the right-hand side accounts for gas heating due to elastic collisions between electrons with neutral species *i* having momentum transfer rate coefficient k_{mi}. Franck-Condon heating due to electron impact dissociative processes is accounted for by the third term, where $\Delta\varepsilon_i$ is the translational energy released due to dissociation for reaction *i*, having total rate R_i. The fourth term accounts for heating from the change in enthalpy, ΔH_i, due to heavy particle reactions *i*. The fifth term represents change in enthalpy due to flow into and out of the reactor, where subscript *0* indicates the value for properties flowing into the reactor. The final term accounts for thermal conduction to surfaces, where κ is the thermal conductivity and T_w is the wall temperature.

The ion temperature is elevated above the gas temperature due to acceleration in the radial ambipolar electric fields that confine the plasma. Due to the high collisionality at atmospheric pressure, the ions are only a few tens of degrees higher in temperature than the neutrals.

The electron temperature, $T_e = \frac{2}{3k_B}\varepsilon$, where ε is the average electron energy, is resolved by integration of the electron energy equation,

$$\frac{\partial\left(\frac{3}{2}n_e k_B T_e\right)}{\partial t} = P_e - n_e\sum_{i,j}\Delta\varepsilon_{ij}k_{ij}N_i + \sum_{i,j}\Delta\varepsilon_{ij}k_{ij}N_iN_j - \sum_i \frac{3}{2}n_e N_i k_{mi}\left(\frac{2m_e}{M_i}\right)k_b\left(T_e - T_i\right) \tag{4}$$

where n_e is the electron density and P_e is the power deposition into electrons. The second term represents the energy loss or gain due to inelastic collisions, where $\Delta\varepsilon_{ij}$ is the change in energy that occurs during collision *j* with species *i* having density N_i during a process with reaction rate coefficient k_{ij}. The change in energy $\Delta\varepsilon_{ij}$ is negative for inelastic collisions and positive for superelastic collisions. The third term is a source term due to collisions between gas phase species N_i and N_j that produces an electron with energy $\Delta\varepsilon_{ij}$. The final term represents power loss by elastic collisions between electrons and neutral atoms and ions. When modeling the APPJ using plug flow, P_e is specified as a function of axial position.

Electron impact rate coefficients were obtained by solving Boltzmann's equation for the stationary electron energy distribution for a range of E/N (electric field/gas number density), and creating a lookup table of rate (and transport) coefficients as a function of electron temperature. This table was then interpolated during execution of the model. The table was periodically updated as the mole fractions of species change.

The APPJ was operated in the steady state. When modeling the APPJ using plug flow, Eq. 1-4 are integrated in time, or equivalently along the length of the plasma column, until reaching the surface of the liquid. At this point, the plasma flow is terminated and the current plasma fluxes for charged and neutral species are directed onto the liquid surface. The liquid surface then appears as one of the surfaces in Eq. (1). The calculation of liquid phase densities in the liquid module is described in Ref.[21]. Briefly, the liquid module contains liquid-phase species and a reaction mechanism distinct from the gas phase. The gas-liquid interface is treated as a material surface to which species diffuse in both the gas and liquid phases. The sticking coefficient for the diffusion loss of neutral species from the gas to the surface representing the liquid represents the loss of gas phase species solvating into the liquid. This sticking coefficient is determined by Henry's law of equilibrium. For species i, the effective sticking coefficient, S_i on the liquid is

$$S_{il} = \max\left(\frac{h_i n_{ig} - n_{il}}{h_i n_{ig}}, 0\right) \tag{5}$$

where n_{ig} is the gas phase density of species i, n_{il} is the liquid phase density of species i, and h_i is the Henry's law constant. As long as the liquid is not saturated ($n_{il}/n_{ig} < h_i$), S_{il} has a non-zero value, meaning that there can be a net flux of gas phase species into the solution. The flux of species i from the jet into the liquid is then

$$\Gamma_i^l = n_{ig} S_{il} \frac{D_{ig}}{\Lambda_b} \tag{6}$$

where Λ_b is the diffusion length across the boundary layer between the jet and the liquid surface, and D_{ig} is the gas phase diffusion coefficient.

If the liquid becomes oversaturated, then species transport from the liquid to the gas with flux

$$\Gamma_i^g = \frac{D_{il}\left(n_{i,l} - h_i n_{i,g}\right)}{\Lambda_b} \tag{7}$$

where D_{il} is the liquid phase diffusion coefficient. Henry's Law constants used in this work are the same as listed in Ref. [21]. All gas phase charged species and electrons that impinge upon the liquid immediately solvate. The time rate of change of the density of liquid species i is given by:

$$\frac{dn_i}{dt} = \sum_j \left\{ \left(a_{ij,R} - a_{ij,L}\right) k_j \prod_l n_l^{a_{lj,L}} \right\} + \left(\Gamma_i^l - \Gamma_i^g\right) \frac{A_l}{V_l} \tag{8}$$

where the interfacial area of the liquid is A_l and the liquid volume is V_l. The first term represents sources or losses of species i through liquid-phase reactions j. The second term accounts for solvation and de-solvation of species.

To distinguish between species that can exist both in the gas phase and in solution, the in-solution species carry an "aq" subscript. For example, H_2O_2 is a gas phase species and H_2O_{2aq} is an in-solution or aqueous species. The exception is Ag_n^{m+} that exist only in solution, and do not carry the "aq" subscript.

III. Silver Growth Pathways and Reaction Mechanism

The Ag reaction mechanism was developed using a data tree-based mapping technique that is described below. Electronic energies for the mapping technique were computed using DFT at the TPSS[22]/def2-QZVP[23] level with D3BJ [24] dispersion corrections in SMD continuum water [25]. This level of theory has previously been shown to generate sufficiently accurate Ag nanocluster energies [26]. The absence of imaginary vibrational frequencies was used to confirm that each structure was at an energetic minimum. All DFT computations were performed using ORCA [27].

The *PathTree* data tree approach described elsewhere [28] was utilized to generate all possible reactions in the growth of neutral and cationic silver clusters starting with a given reactant set based on Ag^+. In these reaction data trees, each node represents the product of a reaction between the previous step's product and a reactant defined by the connecting edge and begins with the starting material as the “root” node. In this manner, we can take a starting material, such as Ag^+, and a defined set of reactants of interest, such as silver nanoclusters with specific size range and charge, and then systematically map every possible reaction between the starting species and those reactants, and each subsequent product and the selected reactants. Here the full reactant set is defined as Ag_n^m where n = 1-9 atoms and m = 0 to 3+. The maximum allowed cluster size for products was set to nine atoms, with a maximum allowed charge of +3. Only the minimum energy structure for each set of n,m was considered. A subset (described in more detail below) of these reactions is shown in Fig. 1.

The initial steps of a typical Ag growth reaction start from the Ag^+ precursor and proceed along one of two thermodynamically favored paths: either the Ag^+ is reduced to Ag^0 (via either reaction with a solvated electron or some other reducing species in solution), which can then dimerize with another Ag^0 to form Ag_2^0, or the Ag^+ is able to react with a previously reduced Ag^0 to form Ag_2^+. The reaction of 2 Ag^+ to form Ag_2^{2+} is thermodynamically unfavorable. We chose these four species, Ag^0, Ag^+, Ag_2^0, and Ag_2^+ as the initial set of reactants to grow the tree. This will also begin the process of producing a reduced reaction set.

To generate a reduced reaction set, the allowed reactants were divided into three major sets; set one consisted of the major products of the initial two reaction sets and the starting material, Ag_1^0, Ag_1^+, Ag_2^0, Ag_2^+; set two consisted of the major products of steps three through five of the mechanism, Ag_3^+, Ag_4^+, Ag_4^{2+}, Ag_5^+, and Ag_5^{2+}; and set 3 consisted of the larger neutral species, Ag_3^0, Ag_4^0, and Ag_5^{0}. To eliminate any potential artificial buildup of Ag^{2+} (a weakly stable species), an additional set of reactions involving Ag^{2+} with all product species was generated. Then, the reaction tree was generated for each of the three reaction sets, but propagation was restricted to include only the two most exothermic reactions at each step in the mechanism. Fig. 1 shows the pruned tree resulting from the Ag_1^0, Ag_1^+, Ag_2^0, Ag_2^+ reaction set, which highlights the two most exothermic reactions at each step. The overall size of the reaction set was reduced without allowing the larger size regime to dominate the system.

Reaction rates for the Ag_n^{m+} - Ag_n^{m+} reactions were computed under the assumption that the rates were diffusion limited. Preliminary efforts at computing the rates via reaction barriers revealed that the Ag-Ag reactions are almost always barrierless, with exceptions involving species that are thermodynamically unstable and thus are not included in the *PathTree* algorithm. This suggests that the solvent controlled diffusion process is the limiting factor in determining the rate of reaction. Diffusion coefficients, D, were calculated for each Ag species as [29,30]:

$$D = \frac{k_b T}{6\pi\eta R} \tag{9}$$

where k_B is Boltzmann's constant, T is the temperature of the system, $\eta = 0.8903$ cP is the viscosity of the solvent at temperature T [31], and R is the maximum radius of the nanocluster. The reaction rate, k, is then calculated based on the size and diffusion-controlled rate constants [32]:

$$k_r = \frac{k_B}{[B]R_{AB}} \tag{10}$$

$$k_D = 4\pi D_{AB} R_{AB} \tag{11}$$

$$k = \frac{k_r k_D}{k_r + k_D} \tag{12}$$

where k_r and k_D are the size and diffusion-controlled components of the rate, A and B are the reacting species, $[B]$ is the concentration of reactant B, R_{AB} is the sum of the nanocluster radii for the reactants, and D_{AB} is the sum of the reactant diffusion coefficients. The nanocluster radii are taken to be half of the longest end-to-end distance. For small silver clusters, the calculated reaction rates were compared to experimentally determined rate coefficients collated in Ref.[17]. Differences were relatively small, approximately a factor of 2, lending credence to the diffusion-limited rate calculations. For example, the rate coefficients derived for $Ag + Ag \rightarrow Ag_2$,1.23×10^{-11} cm^3s^{-1}, and for $Ag^+ + Ag \rightarrow Ag_2^+$,$1.26 \times 10^{-11}$ cm^3s^{-1}, are about half that reported in Ref. [17].

Reaction rates between silver clusters and other aqueous species in solution were calculated based on experimentally determined reaction rates [17] in conjunction with some additional assumptions or modifications. For electron reduction reactions in solution, it was assumed that the reaction rate increased with charge state since the Coulomb attraction becomes larger. That is, the rate coefficient $k(Ag^{m+} + e_{aq}^- + H_2O_{aq} \rightarrow Ag^{m+-1} + H_2O_{aq})$ scales with m. (The "aq" subscript denotes an aqueous or in solution species.) Nanoparticle growth reactions included nucleation, surface growth, and agglomeration of neutral clusters. These reactions took the form of $Ag_n + Ag_j \rightarrow NP$, $n + j > 9$ (nucleation); $Ag_n + NP \rightarrow NP$, $n \leq 9$ (surface growth); and NP + NP → NP (agglomeration). Ion-ion neutralization between $O_2^-{}_{aq}$ and Ag_n^{m+} was included with a fixed reaction rate of $k = 1 \times 10^{-13}$ cm^3 s^{-1} for all cluster sizes in the base case. This value is considered a practical upper limit given the small number of experimental and theoretical values in the literature. The rate coefficient for $Ag + O_2 \rightarrow Ag^+ + O_2^-$ was reduced to 8.30×10^{-14} cm^3/s compared to the value in Ref. [17]. This reduction was made based on observations that nucleation was largely suppressed with the higher rate coefficient for solutions having large oxygen content, an observation that conflicts with experiments.

To identify the role of anionic reducing species in the reduction of Ag^+, rate coefficients for the $Ag_n^+ + O_2^- \rightarrow Ag_n + O_2$ ($n \leq 9$) reaction were derived from electron transfer rates calculated using Marcus theory [33].

$$k = \frac{2\pi H^2}{\hbar\sqrt{4\pi k_B T}} exp\left(-\frac{(\Delta G + \lambda)^2}{4\lambda k_B T}\right) \tag{13}$$

The free energy (ΔG) and reorganization energy (λ) were calculated at the B3LYP-D3/ Def2-SVP level of DFT in dielectric continuum water solvent, and electronic couplings (H) were assumed to be 1 meV (typical value [34,35]). Most of the rate coefficients for clusters of different sizes (up to Ag_9) were found to be on the order of 10 $M^{-1}s^{-1}$ with the average rate coefficient being 21 $M^{-1}s^{-1}$. This result is comparable to the value reported by Jones et al. [15]. The Jones et al experiments reported a 10^4 increase in rate coefficient due to catalysis by silver nanoparticles, but we did not see a catalytic effect for Ag nanoclusters with increasing cluster size up to Ag_9. In any event, even with the 10^4 increase, the resulting rate coefficient is still small enough that O_2^- does not play an important role in the Ag^+ reduction process. This will be demonstrated later in this paper.

The possibility of charged NPs is discussed in Section VI. The full reaction mechanism is listed in Table 1. A portion of the reaction mechanism, primarily highlighting pathways included in Ref.[17], is shown in Fig. 2. In addition to Ag_n^{m+} - Ag_n^{m+} reactions, reactions with OH_{aq} and reduction pathways via reactions with H_2O_{2aq}, HO_{2aq} and H_{aq} were included.

IV. RF Plasma Jet Propagation onto a Silver Nitrate Solution

A schematic of the implementation of the RF APPJ in *GlobalKin* in plug flow mode is shown in Fig. 3. The experiments providing the operating conditions [36] use a He atmospheric pressure plasma jet with a N_2 gas shroud flowing into ambient air onto a $AgNO_3$ solution. To emulate these conditions, He with 100 ppm humid air impurities ($N_2/O_2/H_2O$ = 74/20/6) was flowed into a cylindrical tube (radius 0.1 cm) with a flow rate of 2500 sccm. The tube is 1.0 cm long. Upon exiting the tube, N_2 with 100 ppm humid air impurities was injected into the flow with a flow rate of 15 sccm, which represents the diffusion of N_2 from the shroud into the plume. The injected shroud flow is based on 2-dimensional computational fluid dynamics (CFD) calculations of the jet. The end of the tube is 0.5 cm above the surface of the solution. 100 μm above the liquid surface, 50 sccm of H_2O was introduced into the flow to represent a saturated water vapor layer at the surface of the liquid, a value again estimated from CFD calculations.

The liquid, consisting of 5.0 mM $AgNO_3$ water solution in the base case, had a depth of 500 μm, a volume of 1.74×10^{-2} cm^3, and a fixed temperature of 300 K. The $AgNO_3$ is fully hydrolyzed in the solution, providing initial equal densities of Ag^+_{aq} and $NO_3^-{}_{aq}$ of 3.0×10^{18} cm^{-3}. The total power of the APPJ was 3 W, varying as function of distance as shown in Fig.3 to emulate a touching plasma. Diffusion from the gas to the liquid occurs across the flow boundary layer at the surface of liquid of 15 μm. The liquid was exposed to the plasma treatment for 300 s in the base case.

The evolution of gas phase ions and neutral atoms as a function of position are shown in Fig. 4. Although helium was the primary input gas, ions in the gas phase were dominated by impurities, and there were small densities of He^+ and He_2^+ in the flow. The dominant positive ion is O_2^+ due to rapid charge exchange from He ions and Penning ionization from excited states of He, as well as charge exchange among the impurities (Fig. 4a). The impurities were depleted during transit through the plasma (Fig. 4c) by both direct electron impact and excitation transfer reactions with He species. The density of O and H atoms increased as the flow moved axially through the tube as the impurity densities are low enough that secondary reactions such as ozone formation did not constrain their densities.

Initially, O^-, O_2^-, O^-_3 and OH^- were the dominant negative ions in the system. The densities of O_2^-, O^-_3 and OH^- decrease along the flow direction due to depletion of O_2 and H_2O impurities. As N_2 diffused into the flow from the shroud, NO_x species are formed which leads to formation of NO_x^-. The electron density decreases when the shroud gases are introduced due to both the lower power outside the tube and the more rapid rate of power deposition to the N_2 diffusing into the plume.

There is a significant jump in densities of charged and neutral species in crossing the saturated water vapor layer. The final densities of species at the surface of the liquid are indicated by the horizontal tick-marks in Fig. 4. In the saturated water vapor layer, the density of OH^- increased due to dissociative attachment processes with the water vapor ($e + H_2O \rightarrow OH^- + H$). H_2O^+ was formed dominantly by direct electron impact ionization of H_2O ($e + H_2O \rightarrow H_2O^+ + e + e$). H_2O^+ was then quickly depleted by the formation of H_3O^+ ($H_2O + H_2O^+ \rightarrow H_3O^+ + OH$ and $OH + H_2O^+ \rightarrow H_3O^+ + O$) which was the dominant positive ion near the liquid surface. OH increased rapidly in the saturated vapor layer due to electron impact dissociation of H_2O ($e + H_2O \rightarrow OH + H + e$), and its increase resulted in the formation of additional H_2O_2 ($OH + OH \rightarrow H_2O_2$).

The liquid phase densities during the first second of exposure to the plasma are shown in Fig. 5. The density of H_2O_{2aq} is largely due to solvation from the gas phase and reactions of OH_{aq}. The initial density of Ag^+ rapidly decreases due to reduction and subsequent reactions with Ag_n and solvated ROS. Ag^+ is reduced to Ag dominantly by reactions with e_{aq}, and H_{aq}. For these conditions, reduction of Ag^+ is dominated by H_{aq}. Ag is ionized by O_{2aq} to reform Ag^+. A competing path to reduction of Ag^+ is formation of $AgOH^+$ by reaction with OH_{aq}, which also has a branch to Ag^{2+}. Reaction of $AgOH^+$ with hydronium ($H_3O^+{}_{aq}$) produces Ag^{2+}, which is reduced back to Ag^+ by reactions with H_2O_{2aq}, HO_{2aq}, and e_{aq}. (See Fig. 2.) This is a bit of circular chemistry that does not directly lead to nucleation. The circular chemistry is broken by reaction of Ag with Ag to form Ag_2, and Ag with Ag^+ to form Ag_2^+. With large enough densities of Ag_2 and Ag_2^+, reactions of these species lead to formation of higher order Ag_n.

A significant transition occurs in the densities of solvated species upon depletion of Ag and Ag^+. With the depletion of Ag, the formation of $AgOH^+$ decreases which eliminates a loss for OH_{aq}. The increase in OH_{aq} then supports the formation of H_2O_{2aq}. With depletion of Ag^+, a loss for H decreases and so its density increases. Reaction of H with O_{2aq} then enables an increase in the density of HO_{2aq}. With the depletion of Ag^{2+}, losses of H_2O_2 and HO_2 by reaction with Ag^{2+} decrease, enabling an increase in their densities. With the increase in HO_{2aq}, reaction with H_2O then increases the density of $O_2^-{}_{aq}$. These dynamics are in part a result of OH_{aq} and H_2O_{2aq} having reactions only with Ag^{m+} in this mechanism. It is likely that similar reactions occur with Ag_n^{m+}, n > 1. If so, then the sensitivity of nanoparticle formation to in solution ROS would be greater than that discussed here.

V. Nanoparticle Nucleation and Growth

Upon depletion of Ag and Ag^+, the cascade of nucleation and growth reactions that lead to formation of nanoparticles (NPs) then begins. The densities of selected Ag_n, Ag_n^{m+} and NP, and radius of the NPs are shown in Fig. 6 for the base case conditions. Selected densities of neutral Ag_n and NP are shown in Fig. 6a, with the radius of the NP. Dominant ions are shown in Figs. 6b and 6c on different time scales for clarity. The cascade of charge exchange and nucleation reactions (the reduced version of which appears in Fig. 2), sequentially populates larger clusters which are dominantly in their ion state. Due to the NPs in this mechanism being neutral, the density of NPs remains small as long as Ag_n are dominated by cations. As long as Ag^+ has a significant density (the initial density being 3×10^{18} cm^{-3}), small Ag_n^+ are continually produced by through the circular chemistry linking Ag^+, Ag^{2+} and $AgOH^+$, or by reduction to Ag. With this continuous source of small Ag_n, clusters on the average tend to remain small. In particular, the density of neutral Ag_n (n > 1) remains small as reduction reactions are dominated by Ag^+ having the far larger density.

When Ag^+ is depleted (at approximately t = 0.3 – 0.4 s) the source of small Ag_n is eliminated and reducing species (e_{eq}, H_{aq}) are made available for reaction with Ag_n^+. These transitions then enable large neutral Ag_n (n > 4) to nucleate. Since the source of Ag has been eliminated, its density becomes negligible, and so the source of neutral Ag_n is largely due to the reduction of Ag_n cations (as opposed to true nucleation reactions of neutral Ag species). In the absence of a source of Ag to feed the nucleation cascade from the bottom, the growth of large Ag_n (0.3 s < t < 10 s) proceeds following the path from the upper-left to bottom-right in Fig. 1. Reduction of Ag_n^+ produces a neutral (or lower charge state) Ag_n, which then enables a nucleation reaction with Ag_k^{m+}

producing a larger cluster Ag_{k+n}^{m+}. The process continues to form large densities of neutral and cation Ag_8 and Ag_9 having their maximum densities at t = 20-30 s.

The next steps in the cascade to form NPs are an outcome of our model. In this reaction mechanism, $Ag_{n>9}$ are grouped into a single, neutral NP species. Further growth of clusters with $Ag_{n>9}$ in the nucleation cascade then produce NP. The density of NPs rise abruptly at t=7-8 s, with an NP radius of < 1 nm. The large increase in NP density while the radius remains small indicates that growth of NPs is largely due to the initiating nucleation reactions ($Ag_n + Ag_m \rightarrow NP$, $n + m > 9$) and not by surface growth ($Ag_n + NP \rightarrow NP$) or agglomeration. Once NPs are formed, Ag_n, $n \leq 9$, begin to become depleted by growth reactions with the NPs. As long as the NP density continues to increase, the formation of NPs is dominated by nucleation reactions which increase its density ($Ag_n + Ag_m \rightarrow NP$) and not by growth or agglomeration ($NP + NP \rightarrow NP$). The production of NPs by growth and agglomeration increases the radius of the NP without increasing its density.

With only neutral Ag_n contributing to growth reactions of NPs, the nucleation cascade (Fig. 1) is then limited by the availability of neutral Ag_n, which begin to become depleted by t=30-40 s. Upon depletion of neutral Ag_n clusters, the nucleation reactions that produce new NPs are eliminated which corresponds with the peak density of NPs at about the same time. For times t > 50-60 s, nucleation reactions no longer contribute to NP growth, and agglomeration becomes the dominant NP formation process. Agglomeration reactions increase the radii of the NPs while decreasing their density. After 300 s of plasma exposure, the NP radius increases to about 35 nm through agglomeration reactions, while decreasing the NP density from its maximum of 10^{14} cm^{-3} (radius 4 nm) to 8×10^{11} cm^{-3}.

The total inventory of Ag^+ in the reaction layer is 1.5×10^{17} cm^{-2}. In order for solvated electrons to be fully responsible for reduction of the total reduction of Ag^+, the fluence of electrons from the gas phase into solution must be at least the value of the inventory of Ag^+. For the base case conditions, the fluence of electrons onto solution when 99% of Ag_n^+ has been reduced to neutrals (in the form of either Ag_n or NP) is 8.5×10^{16} cm^{-2}. (The time at which 99% of Ag_n^+ has been reduced to neutrals is called the time for full-reduction.) For these conditions, significant reduction has been performed by H_{aq}. The possible role of reduction by reactions with anions is discussed below.

Initially, the solution has pH = 7. In the absence of other reactions, this condition is maintained by balancing reactions ($OH^-_{aq} + H_3O^+_{aq} \leftrightarrow H_2O_{aq} + H_2O_{aq}$) in the based reaction mechanism for plasma activated water [21]. No additional salts or buffers were used to maintain this pH so that we could isolate the role of plasma produced species on NP formation. For the conditions examined, HNO_x species are produced in the plasma plume which then solvate into the solution and hydrolyze, producing $H_3O^+_{aq}$ and $NO_x^-{}_{aq}$. Formation of $NO_x^-{}_{aq}$ does not significantly affect the equilibrium between Ag^+_{aq} and $NO_3^-{}_{aq}$, with $AgNO_{3aq}$ because the equilibrium constants greatly favor the dissociation products. Formation of $H_3O^+_{aq}$ does acidify the solution. For the base case after 100 s of plasma exposure, the acidification is pH = 2.1. This acidification is accounted for in the reaction mechanism by explicitly including the dependence of reaction rates on the density of $H_3O^+_{aq}$. That said, the acidification does not directly affect the NP clustering process.

As discussed in Section III, a reduced reaction set was also developed using data tree mapping. The reduced reaction set contained 127 silver reactions in lieu of 194 reactions in the full reaction set. All of the reactions in Table 1 are included in the full reaction mechanism. A subset of those reactions were excluded in the reduced mechanism, as indicated in the third column. The reactions in the reduced set are indicated in Table 1. A comparison of the full and reduced mechanism for densities of selected species and NP properties is in Fig. 7. Depletion of Ag^+ occurred later and nucleation processes occurred more rapidly with the reduced mechanism compared to the full reaction set. There are significant densities in intermediate species, which is largely due to the steep time derivatives in the initiating species (e.g., Ag^+, Ag_2^+) that then determine which branch of the clustering hierarchy is taken. However, the final NP density and radius are nearly the same for the two mechanisms. These results indicate that pathways selected based on being thermodynamically favorable may also be kinetically favorable.

Overall, the primary reduction and growth pathways for the reduced mechanism were similar to those based on the full reaction set, but there were some notable differences. For example, Ag_4^{2+} persisted in solution longer for the reduced reaction set, as the reduced mechanism had fewer depletion reactions at early times. This may be attributed to Ag_4^{2+} exhibiting additional stability due to sigma aromaticity, or the sharing of 4e+2 (e = 0) valence electrons in sigma type bonds [26]. While this increased stability leads to preferential formation, it also decreases the exothermicity of reactions where sigma aromatic species are reactants. As a result, reactions with sigma aromatic species as reactants are more likely to be removed from the reduced reaction mechanism. Since several sequential reactions in the full reaction set were removed in the reduced mechanism, smaller clusters did not necessarily neutralize prior to larger clusters.

In both reaction sets, the final nanoparticle density and radius critically depend on the rate coefficient for agglomeration (NP + NP → NP). After depletion of Ag_n clusters, agglomeration is the remaining process for growth of the NPs. The rate coefficient for this process in the base case, $k_{ag} = 1.5\times10^{-14}$ cm^3 s^{-1}, was estimated based on analogous reactions of radical species with larger clusters and for producing a NP radius in alignment with experiments. Although silver nanoparticles may have different average radii depending on their structures, a diameter of 30-40 nm agreed reasonably well with experiments for similar conditions [6,37,38,39]. NP density and radius are shown Fig. 8 while varying k_{ag} from 1.5×10^{-16} cm^3 s^{-1} to 1.5×10^{-11}. The time at which the NP density is maximum (t = 30-40 s) is not terribly sensitive to the value of k_{ag} as this time is determined by the depletion of Ag_n forming clusters. At this time larger k_{ag} resulted in lower densities (by a factor of 30) and larger radii (3 nm to 13 nm) over the range of k_{ag} investigated. Upon entering the agglomeration phase (t > 40 s), larger k_{ag} produced larger NP (75 nm vs 13 nm) and lower NP densities (2×10^{11} cm^3 vs 2×10^{13} cm^3) over the range of k_{ag}. Since there is a finite inventory of Ag atoms, the rate of agglomeration determines the distribution of those atoms as NPs. Smaller rates of agglomeration produce larger densities of smaller particles. Larger rates of agglomeration produce smaller densities of larger particles.

To provide insights into the influence of process variables on the reduction process and NP synthesis, the consequences of solution molarity, gas impurity levels, and applied power were investigated. The concentration of $AgNO_3$ was varied from 0.5 mM to 50 mM, with the resulting Ag_n densities and NP properties shown in Figs. 9 and 10. In all cases, Ag^+ was reduced to negligible levels, though this reduction took more time for high molarity solutions (4.2 s for 50 mM, Fig. 9a) compared to low molarity solutions (0.04 s for 0.5 mM, Fig. 9a,10a). The initial reduction step (from Ag^+ to Ag) produced a larger density of Ag for the lowest molarity solutions. Since the fluence of reducing species into solution from the gas phase was the same for all molarities, the initial rate of reduction of Ag^+ to Ag is actually larger with higher molarity, which should produce a larger density of Ag. However, with a larger molarity, the Ag that is produced is depleted more rapidly by reactions with Ag^+ ($Ag + Ag^+ \rightarrow Ag_2^+$). Larger molarities and larger densities of $NO_3^-{}_{aq}$ also deplete reducing species. For example, the reactions $NO_3^-{}_{aq} + H_{aq} \rightarrow HNO_3^-{}_{aq}$ and $NO_3^-{}_{aq} + H_2O_{aq} + e_{aq} \rightarrow NO_3^{2-}{}_{aq} + H_2O_{aq}$ deplete the densities of reducing species.

The delayed onset to nucleation with higher molarities is also demonstrated by the Ag_n and NP densities shown in Fig. 10. With higher initial inventories of Ag^+ with higher molarity, smaller

$AgOH^+$ and smaller Ag_n^+ ($n \leq 6$) dominate. Only after Ag^+ is depleted do the larger Ag_n^+ ($n \geq 7$) begin to dominate. With the depletion of Ag^+, the density of $AgOH^+$ decreases. The ratio of neutral to cation clusters generally decreases with increasing molarity. Clusters are more likely to react with the larger inventory of cations than be reduced to neutrals. With the initial densities of Ag being larger at lower molarity, nucleation of NPs began earlier with lower molarities (4 s for 0.5 mM compared to 7.4 s for 50 mM). Maximum NP densities were also achieved earlier with lower molarities (0.4 s for 0.5 mM compared to 300 s for 50 mM) though these maximum densities were nearly the same. With a larger inventory of Ag atoms available at larger molarity, agglomeration in the post-nucleation phase should produce larger NPs. However, the delayed onset of agglomeration at the higher molarities results, after 300 s, in the largest NPs being produced at 1-5 mM (35-40 nm).

For a given molarity, fully reducing the inventory of Ag^+ atoms requires a critical fluence of solvating reactants. For this study of NP formation with molarity, the plasma produced reactant fluxes onto the solution are constant. (We acknowledge that the conductivity of the solution, which is proportional to solution molarity, can affect the fluxes of plasma produced reactants onto the solution.) Longer exposure times then produce larger fluences. The fluences of electrons, f_e, and of H and oxygen containing species (H, OH, O, O_3, H_2O_2, HO_2, H_2O^+, H_3O^+), $f_{O\text{-}H}$, were recorded when 99% of Ag_n^+ has been reduced to neutrals (in the form of either Ag_n or NP) which is the full-reduction state. The results are shown in Table 2.

As a measure of electron reduction efficiency, the ratio of electron fluence at full reduction over Ag^+ inventory, $\eta = f_e/I(Ag^+)$ is shown, as is the ratio of time to full reduction divided by molarity, δ. If the system was operating purely linearly, then the time to reduction would scale linearly with molarity. However, δ decreases with molarity, which indicates that the overall reduction process is becoming more efficient at higher molarity in spite of the delay in nucleation. The electron reduction efficiency η decreases with increasing molarity. This indicates that a larger fraction of the reduction is performed by species other than electrons as the molarity increases. This result is partly a consequence of the plasma fluxes incident onto the solution being limited to be charge neutral by ambipolar forces in the RF discharge. This charge neutral requirement significantly decreases the electron current to the surface of the solution compared to dc discharges. Larger electron currents occur for a dc discharge in which the solution acts as the anode.

Oxygen and H containing impurities in the gas phase can impact the nucleation process in several ways through the aqueous species they produce. Large densities of H may promote reduction,

$$Ag^{+} + H_{aq} + H_2O_{aq} \rightarrow Ag \;\; + H_3O^{+}_{aq}\,, \tag{14}$$

as do other ROS species

$$Ag^{2+} + HO_{2aq} + H_2O_{aq} \rightarrow Ag^{+} + O_{2aq} + H_3O^{+}_{aq}\,, \tag{15a}$$

$$Ag^{2+} + H_2O_{2aq} + H_2O_{aq} \rightarrow Ag^{+} + HO_{2aq} + H_3O^{+}_{aq}\,. \tag{15b}$$

Simply having a solution saturated with atmospheric O_2, or generating O_{2aq} in situ, can significantly alter the nucleation process. For example, the ionization of Ag_{aq} by O_{2aq}

$$Ag \;\; + O_{2aq} \rightarrow Ag^{+} + O^{-}_{2aq} \tag{16}$$

slows the rate of reduction. Solutions saturated with O_{2aq} will likely have a delayed onset of nucleation.

In our mechanism, these reactions with ROS are exclusively with Ag^{m+}_{aq}. A significant unknown is the likelihood of analogous reactions of ROS with $Ag_n{}^{m+}{}_{aq}$, n > 1.

Given the potential importance of O-containing impurities in the gas phase producing ROS in solution, the level of air impurities in the helium gas was varied from 20 ppm to 1000 ppm. We acknowledge that an *impurity* level of 1000 ppm, or 0.1%, might be considered an admixture and not an impurity. The mole fractions of the air impurity were $N_2/O_2/H_2O$ = 0.74/0.20/0.06. Ag density and NP properties are shown in Fig. 11 as a function of time for different impurity levels. The rates of small cluster formation generally scale with the impurity level due to the varying densities of ROS in solution, as shown in Fig. 11a by the sum of the density of all $Ag_2{}^{n+}$ cations. From 20 ppm to 1000 ppm, the density of H_2O_{2aq} increases from 9×10^{13} cm^{-3} to 2.4×10^{16} cm^{-3}, HO_{2aq} increases from 1.5×10^{13} cm^{-3} to 3.7×10^{14} cm^{-}while that of H_{aq} increases from 1×10^{14} cm^{-3} to 2.4×10^{16} cm^{-3}. These trends generally increase the densities of charged, small clusters and neutral Ag_{aq}. Due to the increasing plasma density with increasing impurities, the electron fluence onto solution increases by a factor of 1.6 from 20 ppm to 1000 ppm, which then aids in the total rate of reduction. The end result is that plasma jets having larger impurity levels initiate nucleation and NP growth more rapidly, while on average producing larger densities of small NP.

Prior measurements and our computational estimates indicate that the rate coefficient for reduction of Ag^{+}_{aq} by $O_2{}^{-}{}_{aq}$ is small. That said, the majority of cation-anion neutralization reactions based on ionization potential and electron affinity are exothermic. In developing gas phase plasma chemistry reaction mechanisms, it is standard practice to assume that all negative ions neutralize in reactions with all positive ions, provided the ionization potential of the positive ion is greater than the electron affinity of the negative ion. In solution chemistry, ion solvation tends to reduce exothermicity, and reorganization effects that occur during electron transfer can lead to reaction barriers. As discussed in Section III, the rate coefficient for anion reduction by O_2^- was found to be small, making the anion reduction reaction less likely. Even small rate coefficients for these reactions may be influential to the overall reduction process as anion densities other than the original solute can greatly exceed (by many orders of magnitude) the density of solvated electrons. To illustrate these possibilities, the rate coefficient for anion reduction by $O_2^-{}_{aq}$ was varied from 1×10^{-14} cm^{-3} to 1×10^{-11} cm^{-3}, where the smaller of these values is about an order of magnitude higher than the catalyzed value estimated by Jones et al [15], and therefore is an upper bound to what appears to be the experimental value. The anion reduction was applied to all Ag cations,

$$Ag_n^{m+} + O_{2aq}^- \rightarrow Ag_n^{(m-1)+} + O_{2aq} \tag{17}$$

with the same rate coefficient. The purpose of this parameterization is to demonstrate the possible impact of anion reduction and not to suggest that these rate coefficients strictly apply to reduction by $O_2^-{}_{aq}$. The resulting densities and radii of NPs for the base case conditions are shown in Fig. 12.

Increasing the rate coefficient for anion reduction produces a more rapid onset to nucleation and more rapid formation of NPs, while producing larger NPs. For rate coefficients greater than 1×10^{-12} cm^{-3}, reduction is dominated by anions. That is the fluence of solvated electrons at the time of full reduction is less than the initial inventory of the $Ag^+{}_{aq}$. The larger NPs result from there being more growth reactions (neutral Ag_n clusters that add to the neutral NPs). For anion reduction rate coefficients of 1×10^{-13} cm^{-3} and less, reactions with solvated electrons dominate the reduction process. However, even under these conditions, lowering the rate coefficient for anion reduction below 1×10^{-13} cm^{-3} produces a delay in the onset of nucleation and formation of NPs. This offset is due, in part, to the small contribution of anion reduction. However, the majority of this delay is due to the resulting increase in the density of $O_2^-{}_{aq}$ which impacts the density of other ROS species important to the nucleating processes.

Ag density and NP properties are shown in Fig. 13a as a function of power for the base case and for He only plasmas without any impurities in the gas mixture. The expected trends are confirmed – more rapid reduction and nucleation with increasing power due to the increase in electron and ROS fluxes onto the solution surface. Lower powers produced larger densities of smaller NPs due to the lower rates of agglomeration. Although the flux of electrons onto the solution scale approximately with power, the fluxes of ROS onto the solution saturate with power due to the depletion of the impurities. At the highest powers, the impurities are essentially fully dissociated. As a result, more reduction is performed by electrons with increasing power. The initial Ag^+ inventory is 1.5 × 10^{17} cm^{-2} for the 5 mM base. The fluence of electrons at full reduction increases from 2.1 × 10^{16} cm^{-2} for a power of 0.5 W to 1.6 × 10^{17} cm^{-2} for 15 W. At low powers, a larger proportion of the reduction is due to H_{aq} and ROS species. If the process was purely linear, the time required to achieve full reduction would be simply inversely proportional to power. The time required for full reduction at 0.5 W is 267 s, and for 20 W is 37 s, a ratio of 7.2 for a 40 increase in power. (The electron fluxes onto the solution increase by a factor of 48 due to the depletion of the gas impurities.) The reduction process becomes less efficient at higher powers.

NP properties are shown in Figs. 13b,c for He only plasmas with there being no ROS produced in the plasma incident onto the solution for plasma powers of 0.5 to 10 W. This lack of ROS includes, computationally, removing the saturated water vapor about the solution. For a given power, the NP densities are smaller with larger particles for the He only plasmas due to the onset of agglomeration occurring earlier. Comparing the 10 W cases, full reduction requires 26.6 s with an electron fluence of 2.8 × 10^{17} cm^{-2} for the He only plasma compared to 97.5 s and an electron fluence of 1.5 × 10^{17} cm^{-2} for the case with ROS fluxes. This decrease in time is largely a consequence of the electron fluxes being about 3 times larger for the He only plasma. The process is increasingly less efficient at higher powers for the He only plasmas. If the process was purely linear, the fluence of electrons at full reduction would be independent of power. Full reduction would simply take less time. The electron fluence at full reduction at 0.5 W is 1.6 × 10^{17} cm^{-2}, whereas at 10 W the fluence is 2.8 × 10^{17} cm^{-2}.

VI. Alternate Models for NP Synthesis

Several assumptions were made in developing this reaction mechanism for NP synthesis, and in choosing operating conditions. Two of these assumptions will be relaxed here to determine the sensitivity of the mechanism. The first assumption was that the NPs are neutral. This is likely the case after there has been full reduction of the Ag^+ inventory, and NPs grow by agglomeration. However, in the nucleation phase, small NPs likely carry a charge. To test the sensitivity of the mechanism to having charged NPs, the following reactions were added.

$$Ag_n^{m+} + Ag_k \rightarrow NP^{m+}, \quad k+n>9 \tag{18a}$$

$$Ag_n + NP^{m+} \rightarrow NP^{m+} \tag{18b}$$

$$Ag_n^{m+} + NP \rightarrow NP^{m+} \tag{18c}$$

$$NP^{m+} + NP \rightarrow NP^{m+} \tag{18d}$$

$$NP^{m+} + e_s \rightarrow NP^{(m-1)+} \tag{18e}$$

NPs being single, double, and triple charged were included to align with the allowed charge states of the Ag_n clusters. Reactions were not allowed between charged NPs and other charged species to acknowledge the Coulomb barriers. As such, nucleation reactions were only allowed between neutral and charged clusters, to form NPs having the same charge state. Growth reactions were then only allowed between charged clusters and neutral NPs, or charged NPs and neutral clusters resulting in larger NPs of the same charge state. Agglomeration reactions occurred only between neutral and charged NPs to give NPs of the same charge state. Reduction reactions with electrons reduced the charge state of NPs by one.

NP properties and the densities of Ag_9^{n+} for the base case are shown in Fig. 14a for reference. The densities of Ag_9^{n+} are shown as a surrogate for the nucleation cascade. NP properties and the densities of $Ag_9^{n+}$when including charged NPs are shown in Fig. 14b with the sum of the densities of all charged Ag clusters. The densities of charged and neutral NPs and radius of the NPs are shown in Fig. 14c. When including NP^{m+} the formation of nanoparticles occurs at approximately the same time as with only neutral NPs, however these nanoparticles are essentially all charged. During the nucleation cascade leading to NPs, the majority of the Ag_n inventory is charged, which then nucleate with neutral Ag_n to form charged NPs. This leaves a small inventory of neutral Ag_n available to form neutral NPs. Reactions of charged NPs with neutral Ag_n perpetuate the charged NPs. Since the total density of Ag_n^{m+} is large compared to that of the NP^{m+} the limited density of reducing species is expended by reducing the Ag_n^{m+} as opposed to reducing the NP^{m+}. Any neutral Ag_n produced by the reduction then add by surface growth to the NP^{m+}. This process continues until the Ag_n^{m+} population is fully reduced. At this time, reduction reactions are focused on producing neutral NPs which then grow by agglomeration. Although the path to the final NP state is quite different with charged NPs, the final densities and radii are commensurate, with the mechanism with charged NPs ultimately producing larger particles.

The second major assumption made in this study is the charge neutral, ambipolar nature of the charged particle fluxes onto the solution, as would occur in the plume of an RF discharge. This assumption was relaxed by simulating a DC discharge in which the solution is the anode receiving 0.3 to 10 mA/cm^2 of electron current. The resulting NP properties and the densities of all Ag_n^{m+} clusters are shown in Fig. 15. The higher flux of electrons into solution produces a more rapid onset of nucleation and NP formation which ultimately produces about the same size NP. However, the electron fluence at full reduction is about 6×10^{16} cm^{-2} for all currents indicating that only about half the Ag_n^+ is reduced by solvated electrons.

VI. Concluding remarks

A reaction mechanism was developed to describe the reduction of Ag^+ and subsequent nanoparticle (NP) nucleation, growth, and agglomeration in a water-based silver nitrate ($AgNO_3$) solution. The reaction mechanism was first applied to the analysis of an RF atmospheric pressure plasma jet whose charge neutral, ambipolar limited plume impinges onto an aqueous $AgNO_3$ solution. To develop the reaction mechanism, density functional theory (DFT) was used to generate thermodynamically probable silver growth pathways up to Ag_9, and these pathways were incorporated into a reaction mechanism for use in a global plasma chemistry model. Kinetic reaction rate coefficients for probable growth pathways were estimated based on a combination of existing data and theory. Diffusion-limited reaction rate coefficients were calculated for exothermic reactions that occur between silver clusters and ions, and nanoparticle agglomeration was assumed to begin once a particle cluster contained nine silver atoms. Reactions forming $Ag_{n,}$ $n > 9$ were grouped into a single NP species, which grows by addition of Ag_n (atoms and clusters) and agglomeration.

The global plasma chemistry model was operated in a plug flow mode to assess the impact of operating conditions on the formation of Ag_n clusters and NP formation. Results from the model show that the Ag_n system has an exothermic pathway towards nucleation that can be initiated by moderate amounts of reduction by dominantly solvated electrons. The rate of cascade through the system is somewhat uncertain due to the approximations that needed to be made to convert enthalpies of reaction into rate coefficients. That said, there are no bottlenecks in the cascade that would prevent formation of nanoparticles given sufficient fluences of reducing species. The cascade consists of a series of nucleation reactions that progressively generate mostly charged Ag_n^{m+} which coalesce into NPs. Growth of the NPs then progresses through addition of clusters and agglomeration. Although the rate coefficients for addition of clusters and agglomeration are not precisely known, the values of these coefficients largely only determine the rate of NP growth – and not necessarily the final outcome. The NP growth process is highly sensitive to the rate coefficient for agglomeration.

The role of reactive oxygen species (ROS) and H_{aq} atoms is less clear and more case specific. In most plasma jet treatment of solutions, ROS will be created in the solution by solvation of plasma produced oxygen containing species. Generation of these species is nearly unavoidable due to entrainment of ambient air into the plume, impurities in the gas and water evaporation producing vapor that is dissociated by the plasma. These ROS (HO_{2aq}, and H_2O_2aq in particular) and H_{aq} initiate reduction processes with Ag^+_{aq} while O_{2aq} will ionize Ag_{aq}. In general, large production in solution of ROS and H_{aq} accelerate the reduction process and formation of NPs. A great uncertainty is whether these ROS and H_{aq} reactions also occur with $Ag_n^{m+}{}_{aq}$, large clusters of higher ionization state. If these reactions do indeed occur, the sensitivity on ROS of nanoparticle formation would be even greater than discussed here.

Another poorly understood set of reactions is the role of anions in the reduction process. Energetically, anions are capable of reducing Ag_n^+. Measurements and calculations for Ag^+_{aq} reduction by $O_2^-{}_{aq}$ indicate that this is a slow process, though it is not clear whether that result applies to all Ag_n^{m+} and to other anions. The importance of anion reduction results from the fact that the density of anions in solution (other than that of the solvated solute) can be orders of magnitude larger than the density of solvated electrons. As such even small rate coefficients for anion reduction can have significant effects on NP nucleation.

Another uncertainty is the charge state of NPs. A model for nucleation and growth including charged NPs was discussed. In this model, the vast majority of NPs were charged due to growth processes of charged NPs with neutral clusters that preserved the charge state of the NPs at the expense of the neutral cluster. Agglomeration processes between neutral and charged NPs also preserved the charge state of the charged NPs at the expense of the neutral NP. The density of charged clusters was generally much larger than the density of charged NPs, and so the charged clusters preferentially consumed the reducing species. When the charged clusters were exhausted, the reducing species were then expended in reducing the charged NPs, quickly converting them to neutral NPs.

These trends are fairly universal regardless of the source of reducing species. The cascade through the Ag_n clusters proceeds at a speed which is in large part determined by the fluence of the precursors onto the solution for the reducing species. In this respect, dc current driven NP formation does not significantly differ from RF plasma NP formation other than in the rate of the cascade. Granted, dc current driven systems have larger electron currents and produce larger densities of solvated electrons. However, the cascade is not qualitatively different.

These findings suggest that control of the distribution of NP sizes and densities may lie in pulsed processing or other systems in which the fluence of reducing species onto the solution can be carefully controlled. Once the solution is fully reduced, the formation of NPs is determined by neutral agglomeration rates, over which there is little control other than the use compounds that passivate the surface of the NPs to prevent their agglomeration. The key to controlling the distribution and size of NPs then lies in partial reduction of the solution by metering the fluences of precursors of the reducing agents. This metered delivery is likely best accomplished through pulsed systems in which fixed increments of reducing species are delivered to the solution. The key unknown, however, is the contribution of ROS and anions to this process, and whether those reactions apply to higher order clusters and charge states.

Acknowledgements

Research was sponsored by the Army Research Office and was accomplished under Grant No. W911NF-20-1-0105. The views and conclusions contained in this document are those of the authors and should not be interpreted as representing the official policies, either expressed or implied, of the Army Research Office or the U.S. Government. The U.S. Government is authorized to reproduce and distribute reprints for Government purposes notwithstanding any copyright notation herein. This work was further supported by the National Science Foundation (Nos. 2032604 and 1902878). This material was also based upon work supported by the U.S. Department of Energy, Office of Science, Office of Fusion Energy Sciences under Award No. DE-SC0020232).

Conflict of Interest

The authors have no conflicts of interest to disclose.

Data Availability

The data that support the findings of this study are available from the corresponding author upon reasonable request.

References

1. P. J. Bruggeman *et al*, J. Appl. Phys. **129**, 200902 (2021).
2. P. Vanraes and A. Bogaerts, Appl. Phys. Rev. **5**, 031103 (2018).
3. N. Duran, et al., Nanomedicine 112, 789 (2016).
4. S. Pan *et al*, Ind. Eng. Chem. Res. **58**, 984 (2019).
5. A. GhavamiNejad *et al*, ACS Appl. Mater. Interfaces 7, 12176 (2015).
6. V. S. S. K. Kondeti, U. Gangal, S. Yatom, and P. J. Bruggeman, J. Vac. Sci. Technol. A. **35**, 061302 (2017).
7. C. Richmonds *et al.*, J. Am. Chem. Soc. **133**, 17582 (2011).
8. C. De Vos *et al*, J. Phys. D: Appl. Phys. **50**, 105206 (2017).
9. P. Rumbach and D. B. Go, Top. Catal. **60**, 299 (2011).
10. S. Ghosh, R. Hawtof, P. Rumbach, D. B. Go, R. Akolkar and R. M. Sankaran, J. Electrochem. Soc. **164**, D818 (2017).
11. N. Shirai, S. Uchida and F. Tochikubo, Jpn J Appl Phys **53**, 046202 (2014).
12. J. Patel, L. Nemcava, P. Maguire, W. G. Graham and D. Mariotti, Nanotechnology **24**, 245604 (2013).
13. K. Maity, D. K. Panda, E. Lochner and S. Saha, J. Am. Chem. Soc. **137,** 2812 (2015).
14. F. Dong, C. Wu, A-J. Miao and K. Pan, Environ. Sci. Nano **8**, 269 (2021).
15. A. M. Jones, S. Garg, D. He, A. N. Pham and T. D. Wait, Environ. Sci. Technol. **45,** 1428 (2011)
16. T. Sakai, H. Enomoto, K. Torigoe, H. Sakai, and M. Abe, Colloids and Surfaces A: Physicochem. Eng. Aspects **347**, 18 (2009).
17. Y. Zheng, L. Wang, and P. Bruggeman, J. Vac. Sci. Technol. A **38**, 063005 (2020).
18. O. I. Kuntyi et al., Colloid Polymer Sci. **299**, 855 (2021)
19. G. Aito, C. Zhu and T. Akiyama, Adv. Powder Technol. **25**, 728 (2014).
20. N. T. K. Thanh, N. Maclean and S. Mahiddine, Chem. Rev. **114**, 7610 (2014).
21. A. M. Lietz and M. J. Kushner, J. Phys. D: Appl. Phys. **49**, 42504 (2016).
22. V. N.Staroverov *et al,* J. Chem. Phys. **119,** 12129 (2003).
23. F. Weigend and R. Ahlrichs, Phys. Chem. Chem. Phys. **7**, 3297 (2005).
24. S. Grimme, S. Ehrlich, and L. Goerigk, J. Comput.Chem, **32**, 1456 (2011).
25. A. V. Marenich, C. J. Cramer, and D. G. Truhlar, J. Phys Chem. B. **113,** 6378 (2009).
26. L. O. Jones *et al* Mol. Phys. **119,** 17 (2021).
27. F. Neese, Wiley Interdiscip. Rev. Comput. Mol. Sci **2.** 73 (2012).
28. C. M. Mueller and G.C. Schatz, J. Phys. Chem. A. **126**, 34, 5864 (2022).
29. A. Einstein. Annalen der Physik. **322,** 549 (1905).
30. S. Lee and M. Karplus, J. Chem. Phys. **88**, 4, 1883 (1998)
31. L. Korson *et al*, J. Phys. Chem. **73** 335 (1969).
32. S. Lee and M. Karplus, J. Chem Phys. **86** 1883 (1998).
33. R. A. Marcus, J. Chem. Phys. **24**, 966 (1956).
34. C-I. Wang, I. Joanito, C-F. Lan and C-P. Hsu, J. Chem. Phys. **153,** 214113 (2020).

35. S. Chaudhuri et al., J. Chem. Theory Comput. **13,** 6000 (2017).

36. P. Bruggeman, Private Communication, 2022.
37. T. Habib, J. M. A. Caiut and B. Caillier, Nanotechnology 33, 325603 (2022).
38. A. Treshchalov et al. Plasma Medicine **6**, 85 (2016).
39. D. Tasche et al., Nanomaterials **10,** 555 (2020).

Table 1: Ag Nucleation and NP Formation Reaction Mechanism

Process	Rate Coefficient (cm^{-3}/s, cm^{-6}/s)	Included in Reduced Mechanism y = yes, n = no	Reference (this work unless noted)
$Ag + Ag \rightarrow Ag_2$	1.23×10^{-11}	y	
$Ag + O_2 \rightarrow Ag^+ + O_2^-$	8.30×10^{-14}	y	[17] (see text)
$Ag^+ + Ag \rightarrow Ag_2^+$	1.26×10^{-11}	y	
$Ag^+ + H + H_2O \rightarrow Ag + H_3O^+$	1.0×10^{-33}	y	[17]
$Ag^+ + OH \rightarrow AgOH^+$	1.99×10^{-11}	y	[17]
$Ag^+ + OH \rightarrow Ag^{2+} + OH^-$	2.49×10^{-11}	y	[17]
$AgNO_3 \rightarrow Ag^+ + NO_3^-$	5.0×10^{-15}	y	
$AgOH^+ + H_3O^+ \rightarrow H_2O + H_2O + Ag^{2+}$	1.99×10^{-11}	y	[17]
$Ag^{2+} + Ag \rightarrow Ag_2^{2+}$	1.30×10^{-11}	y	
$Ag^{2+} + Ag^+ \rightarrow Ag_2^{3+}$	1.24×10^{-11}	y	
$Ag^{2+} + HO_2 + H_2O \rightarrow O_2 + Ag^+ + H_3O^+$	8.49×10^{-36}	y	[17]
$Ag^{2+} + H_2O_2 + H_2O \rightarrow HO_2 + Ag^+ + H_3O^+$	2.25×10^{-36}	y	[17]
$Ag^{2+} + O_2^- \rightarrow Ag^+ + O_2$	5.0×10^{-12}	y	
$Ag^{2+} + (H_2Oe)_S \rightarrow Ag^+ + H_2O$	1.2×10^{-10}	y	
$Ag_2 + Ag \rightarrow Ag_3$	1.25×10^{-11}	n	
$Ag_2 + Ag^+ \rightarrow Ag_3^+$	1.31×10^{-11}	y	
$Ag_2 + Ag^{2+} \rightarrow Ag_3^{2+}$	1.38×10^{-11}	y	
$Ag_2 + Ag_2 \rightarrow Ag_4$	1.23×10^{-11}	n	
$Ag_2^+ + Ag \rightarrow Ag_3^+$	1.25×10^{-11}	y	
$Ag_2^+ + Ag^+ \rightarrow Ag_3^{2+}$	1.32×10^{-11}	n	
$Ag_2^+ + Ag^{2+} \rightarrow Ag_3^{3+}$	1.40×10^{-11}	y	
$Ag_2^+ + Ag_2 \rightarrow Ag_4^+$	1.23×10^{-11}	y	
$Ag_2^+ + Ag_2^+ \rightarrow Ag_4^{2+}$	1.23×10^{-11}	y	
$Ag_2^{2+} + Ag \rightarrow Ag_3^{2+}$	1.49×10^{-11}	y	
$Ag_2^{2+} + Ag_2 \rightarrow Ag_4^{2+}$	1.37×10^{-11}	y	
$Ag_2^{2+} + Ag_2^+ \rightarrow Ag_4^{3+}$	1.36×10^{-11}	n	

$Ag_2^{2+} \rightarrow Ag^+ + Ag^+$	1.0×10^{-6}	y	
$Ag_2^{3+} + Ag \rightarrow Ag_3^{3+}$	1.49×10^{-11}	y	
$Ag_2^{3+} + Ag_2 \rightarrow Ag_4^{3+}$	1.370×10^{-11}	y	
$Ag_3 + Ag \rightarrow Ag_4$	1.26×10^{-11}	y	
$Ag_3 + Ag^+ \rightarrow Ag_4^+$	1.34×10^{-11}	y	
$Ag_3 + Ag^{2+} \rightarrow Ag_4^{2+}$	1.42×10^{-11}	y	
$Ag_3 + Ag_2 \rightarrow Ag_5$	1.24×10^{-11}	y	
$Ag_3 + Ag_2^+ \rightarrow Ag_5^+$	1.23×10^{-11}	y	
$Ag_3 + Ag_2^{2+} \rightarrow Ag_5^{2+}$	1.34×10^{-11}	n	
$Ag_3 + Ag_2^{3+} \rightarrow Ag_5^{3+}$	1.34×10^{-11}	n	
$Ag_3 + Ag_3 \rightarrow Ag_6$	1.23×10^{-11}	y	
$Ag_3^+ + Ag \rightarrow Ag_4^+$	1.25×10^{-11}	n	
$Ag_3^+ + Ag^+ \rightarrow Ag_4^{2+}$	1.32×10^{-11}	y	
$Ag_3^+ + Ag^{2+} \rightarrow Ag_4^{3+}$	1.39×10^{-11}	y	
$Ag_3^+ + Ag_2 \rightarrow Ag_5^+$	1.23×10^{-11}	n	
$Ag_3^+ + Ag_2^+ \rightarrow Ag_5^{2+}$	1.23×10^{-11}	y	
$Ag_3^+ + Ag_2^{2+} \rightarrow Ag_5^{3+}$	1.36×10^{-11}	n	
$Ag_3^+ + Ag_3 \rightarrow Ag_6^+$	1.23×10^{-11}	n	
$Ag_3^+ + Ag_3^+ \rightarrow Ag_6^{2+}$	1.23×10^{-11}	n	
$Ag_3^{2+} + Ag \rightarrow Ag_4^{2+}$	1.26×10^{-11}	y	
$Ag_3^{2+} + Ag^+ \rightarrow Ag_4^{3+}$	1.33×10^{-11}	n	
$Ag_3^{2+} + Ag_2 \rightarrow Ag_5^{2+}$	1.23×10^{-11}	y	
$Ag_3^{2+} + Ag_2^+ \rightarrow Ag_5^{3+}$	1.23×10^{-11}	n	
$Ag_3^{2+} + Ag_3 \rightarrow Ag_6^{2+}$	1.23×10^{-11}	y	
$Ag_3^{2+} + Ag_3^+ \rightarrow Ag_6^{3+}$	1.23×10^{-11}	n	
$Ag_3^{3+} + Ag \rightarrow Ag_4^{3+}$	1.35×10^{-11}	y	
$Ag_3^{3+} + Ag_2 \rightarrow Ag_5^{3+}$	1.28×10^{-11}	y	
$Ag_3^{3+} + Ag_3 \rightarrow Ag_6^{3+}$	1.26×10^{-11}	n	
$Ag_3^{3+} \rightarrow Ag^+ + Ag^+ + Ag^+$	1.0×10^{-6}	y	
$Ag_4 + Ag \rightarrow Ag_5$	1.39×10^{-11}	n	
$Ag_4 + Ag^+ \rightarrow Ag_5^+$	1.56×10^{-11}	y	
$Ag_4 + Ag^{2+} \rightarrow Ag_5^{2+}$	1.70×10^{-11}	y	
$Ag_4 + Ag_2 \rightarrow Ag_6$	1.31×10^{-11}	y	

$Ag_4 + Ag_2^+ \rightarrow Ag_6^+$	1.30×10^{-11}	y	
$Ag_4 + Ag_2^{2+} \rightarrow Ag_6^{2+}$	1.24×10^{-11}	y	
$Ag_4 + Ag_2^{3+} \rightarrow Ag_6^{3+}$	1.24×10^{-11}	n	
$Ag_4 + Ag_3 \rightarrow Ag_7$	1.28×10^{-11}	n	
$Ag_4 + Ag_3^+ \rightarrow Ag_7^+$	1.30×10^{-11}	y	
$Ag_4 + Ag_3^{2+} \rightarrow Ag_7^{2+}$	1.29×10^{-11}	n	
$Ag_4 + Ag_3^{3+} \rightarrow Ag_7^{3+}$	1.24×10^{-11}	n	
$Ag_4 + Ag_4 \rightarrow Ag_8$	1.23×10^{-11}	y	
$Ag_4^+ + Ag \rightarrow Ag_5^+$	1.36×10^{-11}	y	
$Ag_4^+ + Ag^+ \rightarrow Ag_5^{2+}$	1.51×10^{-11}	y	
$Ag_4^+ + Ag^{2+} \rightarrow Ag_5^{3+}$	1.64×10^{-11}	y	
$Ag_4^+ + Ag_2 \rightarrow Ag_6^+$	1.29×10^{-11}	n	
$Ag_4^+ + Ag_2^+ \rightarrow Ag_6^{2+}$	1.28×10^{-11}	y	
$Ag_4^+ + Ag_2^{2+} \rightarrow Ag_6^{3+}$	1.25×10^{-11}	y	
$Ag_4^+ + Ag_3 \rightarrow Ag_7^+$	1.27×10^{-11}	n	
$Ag_4^+ + Ag_3^+ \rightarrow Ag_7^{2+}$	1.28×10^{-11}	n	
$Ag_4^+ + Ag_3^{2+} \rightarrow Ag_7^{3+}$	1.27×10^{-11}	y	
$Ag_4^+ + Ag_4 \rightarrow Ag_8^+$	1.24×10^{-11}	y	
$Ag_4^+ + Ag_4^+ \rightarrow Ag_8^{2+}$	1.23×10^{-11}	n	
$Ag_4^{2+} + Ag \rightarrow Ag_5^{2+}$	1.25×10^{-11}	y	
$Ag_4^{2+} + Ag^+ \rightarrow Ag_5^{3+}$	1.33×10^{-11}	n	
$Ag_4^{2+} + Ag_2 \rightarrow Ag_6^{2+}$	1.23×10^{-11}	y	
$Ag_4^{2+} + Ag_2^+ \rightarrow Ag_6^{3+}$	1.23×10^{-11}	y	
$Ag_4^{2+} + Ag_3 \rightarrow Ag_7^{2+}$	1.23×10^{-11}	n	
$Ag_4^{2+} + Ag_3^+ \rightarrow Ag_7^{3+}$	1.23×10^{-11}	n	
$Ag_4^{2+} + Ag_4 \rightarrow Ag_8^{2+}$	1.30×10^{-11}	y	
$Ag_4^{2+} + Ag_4^+ \rightarrow Ag_8^{3+}$	1.28×10^{-11}	n	
$Ag_4^{3+} + Ag \rightarrow Ag_5^{3+}$	1.26×10^{-11}	y	
$Ag_4^{3+} + Ag_2 \rightarrow Ag_6^{3+}$	1.24×10^{-11}	y	
$Ag_4^{3+} + Ag_3 \rightarrow Ag_7^{3+}$	1.23×10^{-11}	n	
$Ag_4^{3+} + Ag_4 \rightarrow Ag_8^{3+}$	1.290×10^{-11}	n	
$Ag_5 + Ag \rightarrow Ag_6$	1.40×10^{-11}	y	
$Ag_5 + Ag^+ \rightarrow Ag_6^+$	1.57×10^{-11}	n	

$Ag_5 + Ag^{2+} \rightarrow Ag_6^{2+}$	1.72×10^{-11}	y	
$Ag_5 + Ag_2 \rightarrow Ag_7$	1.31×10^{-11}	y	
$Ag_5 + Ag_2^{+} \rightarrow Ag_7^{+}$	1.30×10^{-11}	y	
$Ag_5 + Ag_2^{2+} \rightarrow Ag_7^{2+}$	1.24×10^{-11}	y	
$Ag_5 + Ag_2^{3+} \rightarrow Ag_7^{3+}$	1.24×10^{-11}	n	
$Ag_5 + Ag_3 \rightarrow Ag_8$	1.29×10^{-11}	y	
$Ag_5 + Ag_3^{+} \rightarrow Ag_8^{+}$	1.31×10^{-11}	y	
$Ag_5 + Ag_3^{2+} \rightarrow Ag_8^{2+}$	1.30×10^{-11}	y	
$Ag_5 + Ag_3^{3+} \rightarrow Ag_8^{3+}$	1.24×10^{-11}	n	
$Ag_5 + Ag_4 \rightarrow Ag_9$	1.23×10^{-11}	y	
$Ag_5 + Ag_4^{+} \rightarrow Ag_9^{+}$	1.24×10^{-11}	y	
$Ag_5 + Ag_4^{2+} \rightarrow Ag_9^{2+}$	1.30×10^{-11}	y	
$Ag_5 + Ag_4^{3+} \rightarrow Ag_9^{3+}$	1.29×10^{-11}	n	
$Ag_5^{+} + Ag \rightarrow Ag_6^{+}$	1.41×10^{-11}	n	
$Ag_5^{+} + Ag^{+} \rightarrow Ag_6^{2+}$	1.58×10^{-11}	y	
$Ag_5^{+} + Ag^{2+} \rightarrow Ag_6^{3+}$	1.73×10^{-11}	y	
$Ag_5^{+} + Ag_2 \rightarrow Ag_7^{+}$	1.32×10^{-11}	y	
$Ag_5^{+} + Ag_2^{+} \rightarrow Ag_7^{2+}$	1.31×10^{-11}	y	
$Ag_5^{+} + Ag_2^{2+} \rightarrow Ag_7^{3+}$	1.24×10^{-11}	y	
$Ag_5^{+} + Ag_3 \rightarrow Ag_8^{+}$	1.29×10^{-11}	y	
$Ag_5^{+} + Ag_3^{+} \rightarrow Ag_8^{2+}$	1.31×10^{-11}	y	
$Ag_5^{+} + Ag_3^{2+} \rightarrow Ag_8^{3+}$	1.30×10^{-11}	y	
$Ag_5^{+} + Ag_4 \rightarrow Ag_9^{+}$	1.23×10^{-11}	y	
$Ag_5^{+} + Ag_4^{+} \rightarrow Ag_9^{2+}$	1.24×10^{-11}	y	
$Ag_5^{+} + Ag_4^{2+} \rightarrow Ag_9^{3+}$	1.31×10^{-11}	n	
$Ag_5^{2+} + Ag \rightarrow Ag_6^{2+}$	1.350×10^{-11}	y	
$Ag_5^{2+} + Ag^{+} \rightarrow Ag_6^{3+}$	1.5×10^{-11}	n	
$Ag_5^{2+} + Ag_2 \rightarrow Ag_7^{2+}$	1.28×10^{-11}	y	
$Ag_5^{2+} + Ag_2^{+} \rightarrow Ag_7^{3+}$	1.27×10^{-11}	y	
$Ag_5^{2+} + Ag_3 \rightarrow Ag_8^{2+}$	1.26×10^{-11}	y	
$Ag_5^{2+} + Ag_3^{+} \rightarrow Ag_8^{3+}$	1.28×10^{-11}	y	
$Ag_5^{2+} + Ag_4 \rightarrow Ag_9^{2+}$	1.24×10^{-11}	n	
$Ag_5^{2+} + Ag_4^{+} \rightarrow Ag_9^{3+}$	1.23×10^{-11}	y	

$Ag_5^{3+} + Ag \rightarrow Ag_6^{3+}$	1.34×10^{-11}	y	
$Ag_5^{3+} + Ag_2 \rightarrow Ag_7^{3+}$	1.28×10^{-11}	y	
$Ag_5^{3+} + Ag_3 \rightarrow Ag_8^{3+}$	1.26×10^{-11}	n	
$Ag_5^{3+} + Ag_4 \rightarrow Ag_9^{3+}$	1.24×10^{-11}	n	
$Ag_6 + Ag \rightarrow Ag_7$	1.40×10^{-11}	n	
$Ag_6 + Ag^+ \rightarrow Ag_7^+$	1.57×10^{-11}	n	
$Ag_6 + Ag^{2+} \rightarrow Ag_7^{2+}$	1.71×10^{-11}	y	
$Ag_6 + Ag_2 \rightarrow Ag_8$	1.31×10^{-11}	y	
$Ag_6 + Ag_2^+ \rightarrow Ag_8^+$	1.30×10^{-11}	y	
$Ag_6 + Ag_2^{2+} \rightarrow Ag_8^{2+}$	1.24×10^{-11}	n	
$Ag_6 + Ag_3 \rightarrow Ag_9$	1.29×10^{-11}	n	
$Ag_6 + Ag_3^+ \rightarrow Ag_9^+$	1.30×10^{-11}	n	
$Ag_6 + Ag_3^{2+} \rightarrow Ag_9^{2+}$	1.30×10^{-11}	n	
$Ag_6^+ + Ag \rightarrow Ag_7^+$	1.40×10^{-11}	n	
$Ag_6^+ + Ag^+ \rightarrow Ag_7^{2+}$	1.58×10^{-11}	n	
$Ag_6^+ + Ag^{2+} \rightarrow Ag_7^{3+}$	1.73×10^{-11}	y	
$Ag_6^+ + Ag_2 \rightarrow Ag_8^+$	1.32×10^{-11}	y	
$Ag_6^+ + Ag_2^+ \rightarrow Ag_8^{2+}$	1.31×10^{-11}	y	
$Ag_6^+ + Ag_2^{2+} \rightarrow Ag_8^{3+}$	1.24×10^{-11}	n	
$Ag_6^+ + Ag_3 \rightarrow Ag_9^+$	1.29×10^{-11}	y	
$Ag_6^+ + Ag_3^+ \rightarrow Ag_9^{2+}$	1.31×10^{-11}	n	
$Ag_6^+ + Ag_3^{2+} \rightarrow Ag_9^{3+}$	1.30×10^{-11}	n	
$Ag_6^{2+} + Ag \rightarrow Ag_7^{2+}$	1.41×10^{-11}	n	
$Ag_6^{2+} + Ag^+ \rightarrow Ag_7^{3+}$	1.58×10^{-11}	n	
$Ag_6^{2+} + Ag_2 \rightarrow Ag_8^{2+}$	1.32×10^{-11}	y	
$Ag_6^{2+} + Ag_2^+ \rightarrow Ag_8^{3+}$	1.31×10^{-11}	y	
$Ag_6^{2+} + Ag_3 \rightarrow Ag_9^{2+}$	1.29×10^{-11}	y	
$Ag_6^{2+} + Ag_3^+ \rightarrow Ag_9^{3+}$	1.31×10^{-11}	n	
$Ag_6^{3+} + Ag \rightarrow Ag_7^{3+}$	1.36×10^{-11}	y	
$Ag_6^{3+} + Ag_2 \rightarrow Ag_8^{3+}$	1.29×10^{-11}	y	
$Ag_6^{3+} + Ag_3 \rightarrow Ag_9^{3+}$	1.27×10^{-11}	n	
$Ag_7 + Ag \rightarrow Ag_8$	1.40×10^{-11}	y	
$Ag_7 + Ag^+ \rightarrow Ag_8^+$	1.58×10^{-11}	n	

$Ag_7 + Ag^{2+} \rightarrow Ag_8^{2+}$	1.73×10^{-11}	y	
$Ag_7 + Ag_2 \rightarrow Ag_9$	1.32×10^{-11}	n	
$Ag_7 + Ag_2^{+} \rightarrow Ag_9^{+}$	1.31×10^{-11}	y	
$Ag_7 + Ag_2^{2+} \rightarrow Ag_9^{2+}$	1.24×10^{-11}	n	
$Ag_7^{+} + Ag \rightarrow Ag_8^{+}$	1.40×10^{-11}	n	
$Ag_7^{+} + Ag^{+} \rightarrow Ag_8^{2+}$	1.58×10^{-11}	n	
$Ag_7^{+} + Ag^{2+} \rightarrow Ag_8^{3+}$	1.73×10^{-11}	y	
$Ag_7^{+} + Ag_2 \rightarrow Ag_9^{+}$	1.32×10^{-11}	y	
$Ag_7^{+} + Ag_2^{+} \rightarrow Ag_9^{2+}$	1.31×10^{-11}	y	
$Ag_7^{+} + Ag_2^{2+} \rightarrow Ag_9^{3+}$	1.24×10^{-11}	n	
$Ag_7^{2+} + Ag \rightarrow Ag_8^{2+}$	1.41×10^{-11}	n	
$Ag_7^{2+} + Ag^{+} \rightarrow Ag_8^{3+}$	1.58×10^{-11}	n	
$Ag_7^{2+} + Ag_2 \rightarrow Ag_9^{2+}$	1.32×10^{-11}	y	
$Ag_7^{2+} + Ag_2^{+} \rightarrow Ag_9^{3+}$	1.31×10^{-11}	y	
$Ag_7^{3+} + Ag \rightarrow Ag_8^{3+}$	1.42×10^{-11}	y	
$Ag_7^{3+} + Ag_2 \rightarrow Ag_9^{3+}$	1.32×10^{-11}	y	
$Ag_8 + Ag \rightarrow Ag_9$	1.35×10^{-11}	n	
$Ag_8 + Ag^{+} \rightarrow Ag_9^{+}$	1.5×10^{-11}	y	
$Ag_8 + Ag^{2+} \rightarrow Ag_9^{2+}$	1.63×10^{-11}	y	
$Ag_8^{+} + Ag \rightarrow Ag_9^{+}$	1.40×10^{-11}	y	
$Ag_8^{+} + Ag^{+} \rightarrow Ag_9^{2+}$	1.58×10^{-11}	n	
$Ag_8^{+} + Ag^{2+} \rightarrow Ag_9^{3+}$	1.72×10^{-11}	y	
$Ag_8^{2+} + Ag \rightarrow Ag_9^{2+}$	1.40×10^{-11}	y	
$Ag_8^{2+} + Ag^{+} \rightarrow Ag_9^{3+}$	1.57×10^{-11}	y	
$Ag_8^{3+} + Ag \rightarrow Ag_9^{3+}$	1.42×10^{-11}	y	
Reduction			
$Ag_n^{+} + (H_2Oe)s \rightarrow Ag_n + H_2O$	5.98×10^{-11}	y	[17]
$Ag_n^{2+} + (H_2Oe)s \rightarrow Ag_n^{+} + H_2O$	1.2×10^{-10}	y	
$Ag_n^{3+} + (H_2Oe)s \rightarrow Ag_n^{2+} + H_2O$	1.79×10^{-10}	y	
$Ag_n^{m+} + O_2^{-} \rightarrow Ag_n^{(m-1)+} + O_2$	1.0×10^{-13}	y	
Nucleation			
$Ag_n + Ag_m \rightarrow NP, n + m > 9$	1.5×10^{-11}	y	
$Ag_n + NP \rightarrow NP$	1.5×10^{-11}	y	

Agglomeration			
$NP + NP \rightarrow NP$	1.5×10^{-14}	y	
Charged NPs			
$Ag_k^{m+} + Ag_n \rightarrow NP^{m+}$, $k + n > 9$	1.5×10^{-11}	n	
$Ag_n + NP^{m+} \rightarrow NP^{m+}$	1.5×10^{-11}	n	
$Ag_n^{m+} + NP \rightarrow NP^{m+}$	1.5×10^{-11}	n	
$NP + NP^{m+} \rightarrow NP^{m+}$	1.5×10^{-14}	n	
$NP^{+} + (H_2Oe)_s \rightarrow NP + H_2O$	5.98×10^{-11}	n	
$NP^{++} + (H_2Oe)_s \rightarrow NP^{+} + H_2O$	1.20×10^{-10}	n	
$NP^{+++} + (H_2Oe)_s \rightarrow NP^{++} + H_2O$	1.79×10^{-10}	n	
$NP^{m+} + O_2^{-} \rightarrow NP^{(m-1)+} + O_2$	5.0×10^{-11}	n	

Table 2 – Fluences at the time of Full Reduction of Ag^+ Inventory

Molarity (mM)	f_e (cm^{-2})	$f_{O\text{-}H}$ (cm^{-2})	$I(Ag^+)$ Inventory (cm^{-2})	f_e / $I(Ag^+)$	Time at Full Reduction (s)	Time/Molarity
0.5	1.4×10^{16}	1.5×10^{18}	1.5×10^{16}	0.93	27	1.0
1	2.6×10^{16}	2.8×10^{18}	3.0×10^{16}	0.87	50	0.93
5	8.5×10^{16}	9.6×10^{18}	1.5×10^{17}	0.57	169	0.63
10	1.4×10^{17}	1.5×10^{19}	3.0×10^{17}	0.47	270	0.5
25	2.3×10^{17}	2.6×10^{19}	7.5×10^{17}	0.31	453	0.34

Figure Captions

1. Reaction pathways up to nine atoms. Reactions are reduced to the two most favorable reactions with Ag_1^0, Ag_1^+, Ag_2^0, and Ag_2^+.
2. Schematic of reaction mechanism for small clusters showing reduction pathways.
3. Operating conditions for the global model in plug-flow mode. He with 100 ppm humid air impurities flow from the left. The N_2 shroud (with impurities) is introduced at 1 cm. The humid water vapor layer occurs 100 μm above the liquid layer. Power deposition (3 W total) extends to the liquid.
4. Gas phase densities for the base case as function of position along the flow. a) Electron and negative ion densities, b) positive ion densities and c) neutral RONS (reactive oxygen and nitrogen species). The vertical dashed lines indicate where the N_2 shroud and H_2O saturated vapor are introduced. A jump in densities occurs crossing the water vapor layer. The final densities above the liquid are indicated by the horizontal tick-marks.
5. Densities of aqueous species as a function of plasma exposure time. Densities are shown over different dynamic ranges for clarity.
6. Densities of silver-containing species in solution as a function of plasma exposure time. a) Neutral Ag species; and density and radius of nanoparticles (NP), b) densities of silver ions, and c) density of silver ions on an expanded time scale. In (b) the density of NPs are scaled down by a factor of 10.
7. Comparison of selected densities and NP properties (density and radius) for the full reaction mechanism and the reduced mechanism as a function of plasma exposure time. $\sum Ag_5^{m+}$ indicates, for example, the sum of all Ag_5 cations.
8. Nanoparticle (NP) properties as a function of plasma exposure time for different rate coefficients for agglomeration. a) Density of NP and b) radius of NP.
9. Process properties as a function of plasma exposure time for different molarities (mM) of the $AgNO_3$ solution. a) Ag^+ density and radius of nanoparticles (NP), b) NP density and c) selected neutral Ag_n and NP densities for 1 mM and 25 mM solutions.
10. Charged Ag cluster and NP densities as a function of plasma exposure time for $AgNO_3$ solution molarities of a) 0.5 mM, b) 5 mM and c) 25 mM. The left vertical line indicates the time when the NP densities are maximum. The right vertical line indicates the time when full reduction occurs.

PLEASE CITE THIS ARTICLE AS DOI: 10.1063/5.0127568

11. Process properties as a function of plasma exposure time for different levels of humid air impurities. a) Ag_2^{m+} (sum of all Ag_2 cations) density and radius of nanoparticles (NP), and b) NP density.
12. Nanoparticle (NP) properties as a function of plasma exposure time for different rate coefficients for anion reduction. a) Density and b) radius.
13. Nanoparticle (NP) properties as a function of plasma exposure time for different plasma powers. a) NP density and radius for base case conditions with for powers of 0.5 – 20 W. b) NP density with He only plasma for powers of 0.5 – 10 W, and c) NP radius for He only plasma.
14. Process properties as a function of plasma exposure time for different process scenarios. a) Ag_9 cation densities, NP density and Np radius for the a) base case and b) with charged NPs. $\sum Ag_n^{m+}$ indicates the sum of all charged Ag species. c) Densities of charged NPs, neutral NPs and radius of NPs.
15. Process properties as a function of plasma exposure time for DC plasma for electron current onto the solution of 0.3 to 10 mA/cm^2. a) NP density and $\sum Ag_n^{m+}$ indicating the sum of all charged Ag species. b) NP radius and $\sum Ag_n^{m+}$.

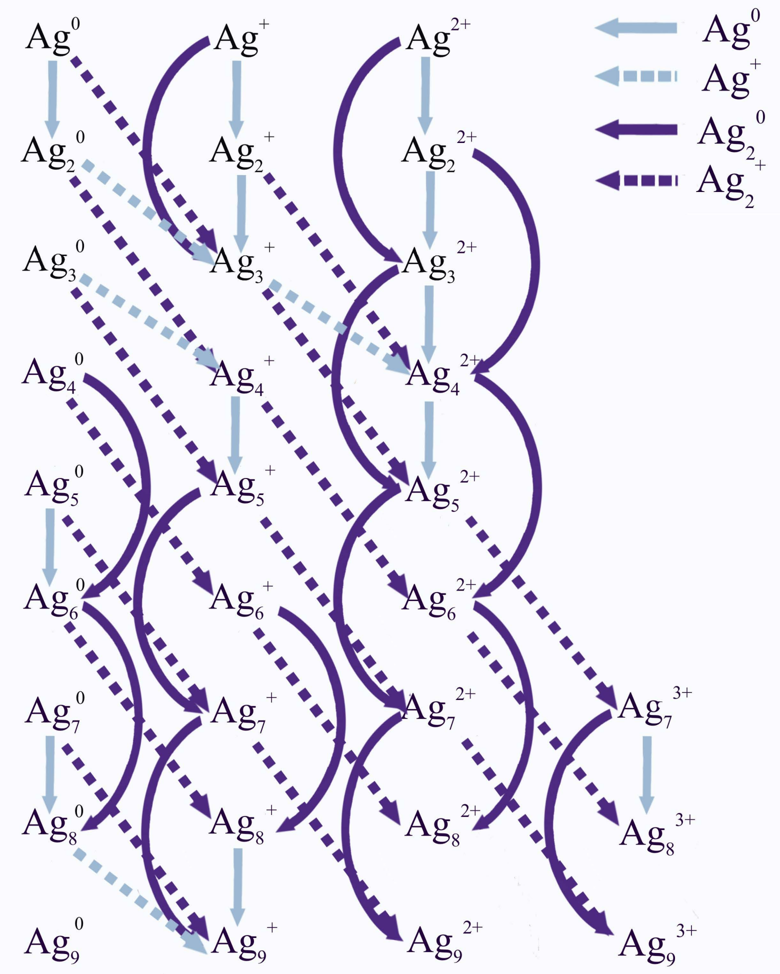
Ag^0
Ag^+
Ag^{2+}
Ag_2^0
Ag_2^+
Ag_2^{2+}
Ag_3^0
Ag_3^+
Ag_3^{2+}
Ag_4^0
Ag_4^+
Ag_4^{2+}
Ag_5^0
Ag_5^+
Ag_5^{2+}
Ag_6^0
Ag_6^+
Ag_6^{2+}
Ag_7^0
Ag_7^+
Ag_7^{2+}
Ag_7^{3+}
Ag_8^0
Ag_8^+
Ag_8^{2+}
Ag_8^{3+}
Ag_9^0
Ag_9^+
Ag_9^{2+}
Ag_9^{3+}
Ag^0
Ag^+
Ag_2^0
Ag_2^+

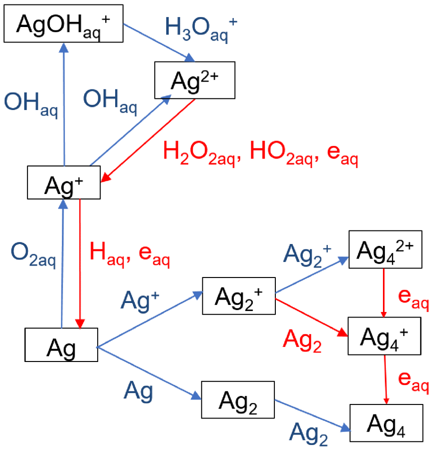
$AgOH_{aq}^+$
$H_3O_{aq}^+$
Ag^{2+}
OH_{aq}
OH_{aq}
H_2O_{2aq}, HO_{2aq}, e_{aq}
Ag^+
O_{2aq}
H_{aq}, e_{aq}
Ag_2^+
Ag_4^{2+}
Ag^+
Ag_2^+
Ag_2^+
e_{aq}
Ag
Ag_2
Ag_4^+
e_{aq}
Ag
Ag_2
Ag_2
Ag_4

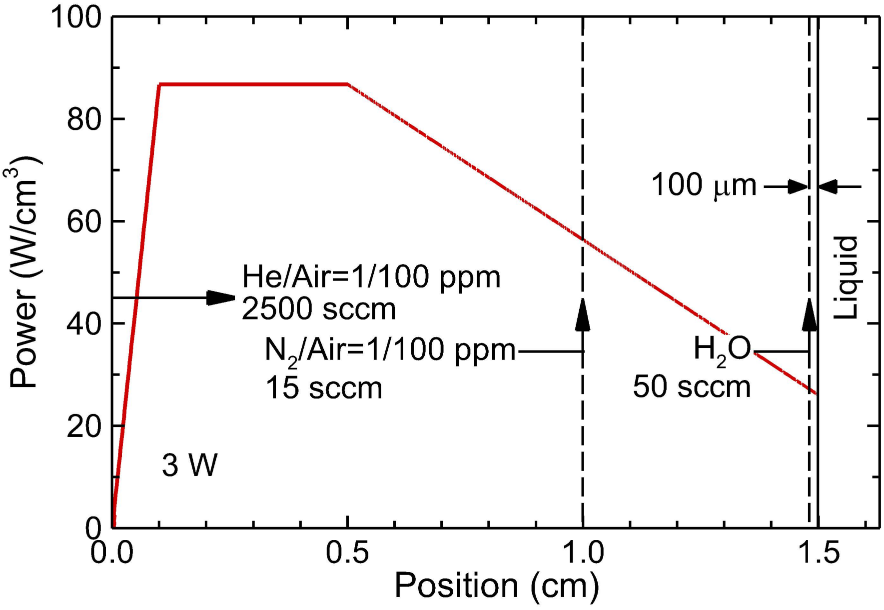
Power (W/cm^3)
0
20
40
60
80
100
Position (cm)
0.0
0.5
1.0
1.5
He/Air=1/100 ppm
2500 sccm
N$_2$/Air=1/100 ppm
15 sccm
H$_2$O
50 sccm
100 μm
Liquid
3 W

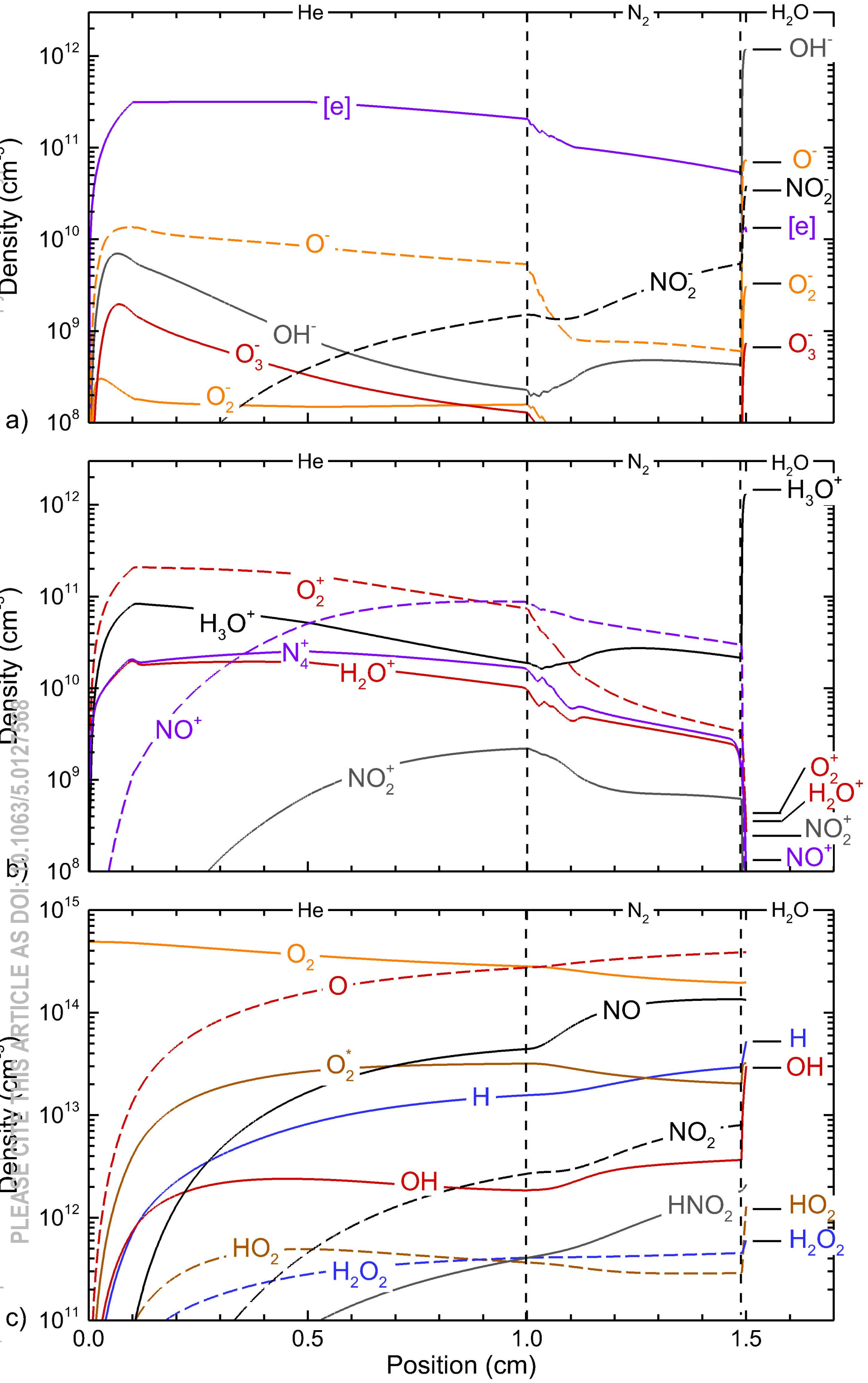
He
N_2
H_2O
a)
b)
c)
Density (cm^{-3})
10^{8}
10^{9}
10^{10}
10^{11}
10^{12}
10^{13}
10^{14}
10^{15}
[e]
O^-
OH^-
O_3^-
O_2^-
NO_2^-
H_3O^+
O_2^+
N_4^+
H_2O^+
NO^+
NO_2^+
O_2
O
NO
O_2^*
H
OH
NO_2
HNO_2
HO_2
H_2O_2
0.0
0.5
1.0
1.5
Position (cm)

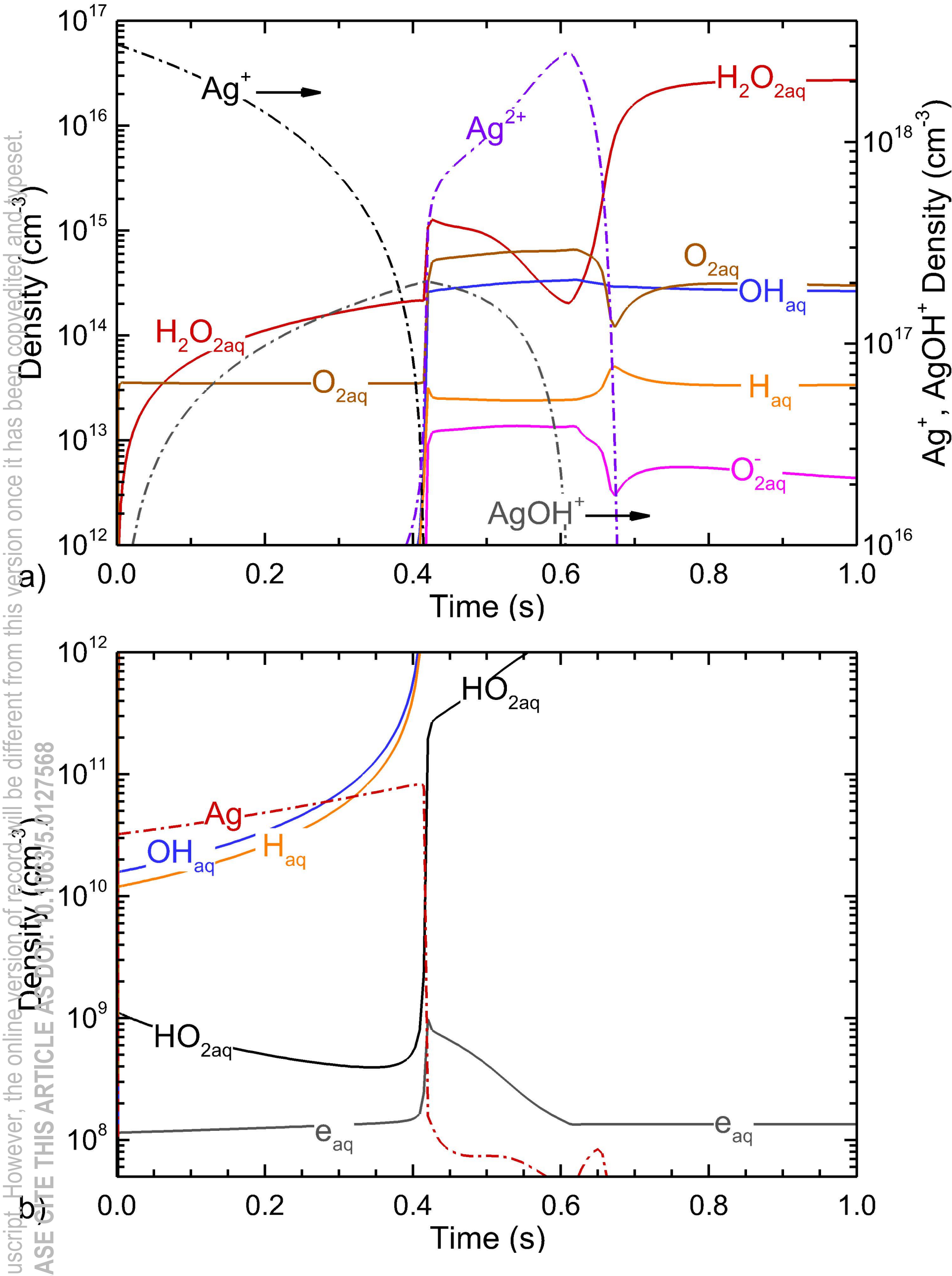
a)
Density (cm-3)
Ag+, AgOH+ Density (cm-3)
10^17
10^16
10^15
10^14
10^13
10^12
10^18
10^17
10^16
Ag+
Ag2+
H2O2aq
O2aq
OHaq
H2O2aq
O2aq
Haq
O-2aq
AgOH+
0.0
0.2
0.4
0.6
0.8
1.0
Time (s)
b)
Density (cm-3)
10^12
10^11
10^10
10^9
10^8
HO2aq
Ag
OHaq
Haq
HO2aq
eaq
eaq
0.0
0.2
0.4
0.6
0.8
1.0
Time (s)

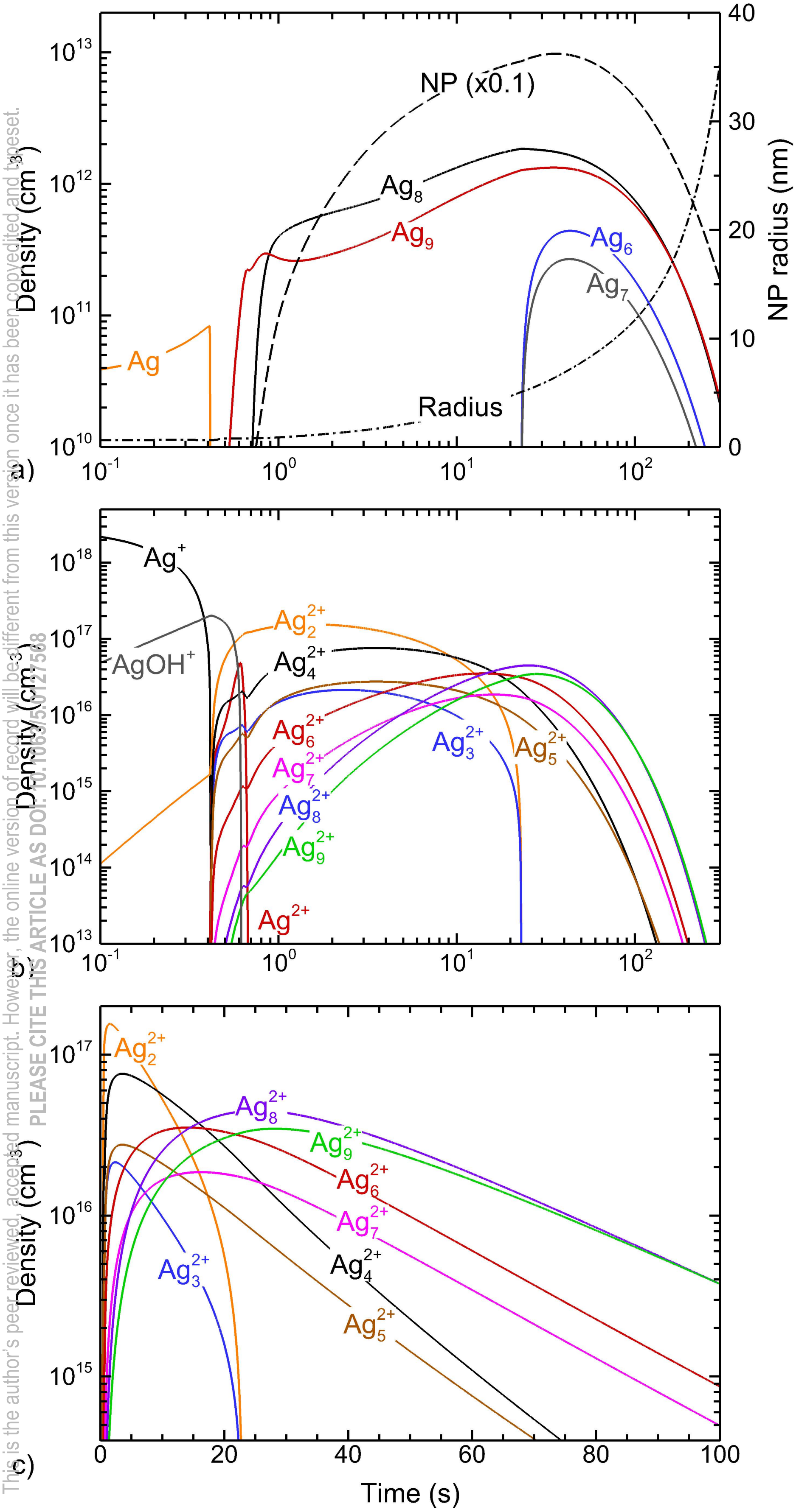
a)
Density (cm^{-3})
NP radius (nm)
10^{10}
10^{11}
10^{12}
10^{13}
0
10
20
30
40
NP (x0.1)
Ag_8
Ag_9
Ag_6
Ag_7
Ag
Radius
10^{-1}
10^{0}
10^{1}
10^{2}
b)
Density (cm^{-3})
10^{13}
10^{14}
10^{15}
10^{16}
10^{17}
10^{18}
Ag^+
$AgOH^+$
Ag_2^{2+}
Ag_4^{2+}
Ag_6^{2+}
Ag_7^{2+}
Ag_8^{2+}
Ag_9^{2+}
Ag^{2+}
Ag_3^{2+}
Ag_5^{2+}
10^{-1}
10^{0}
10^{1}
10^{2}
c)
Density (cm^{-3})
10^{15}
10^{16}
10^{17}
Ag_2^{2+}
Ag_8^{2+}
Ag_9^{2+}
Ag_6^{2+}
Ag_7^{2+}
Ag_4^{2+}
Ag_3^{2+}
Ag_5^{2+}
0
20
40
60
80
100
Time (s)

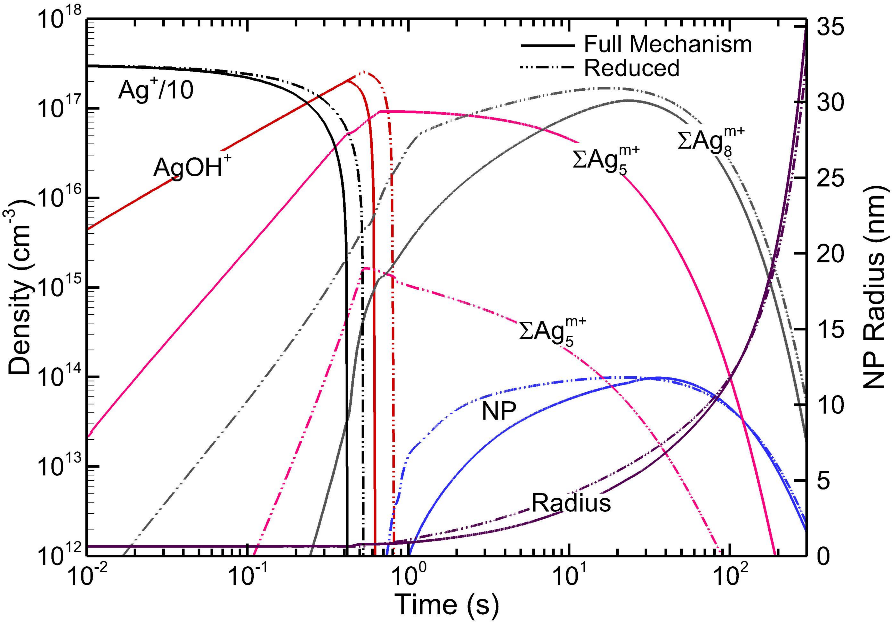
Full Mechanism
Reduced
Ag+/10
AgOH+
ΣAg5m+
ΣAg8m+
ΣAg5m+
NP
Radius
Density (cm-3)
NP Radius (nm)
Time (s)
10^18
10^17
10^16
10^15
10^14
10^13
10^12
10^-2
10^-1
10^0
10^1
10^2
35
30
25
20
15
10
5
0

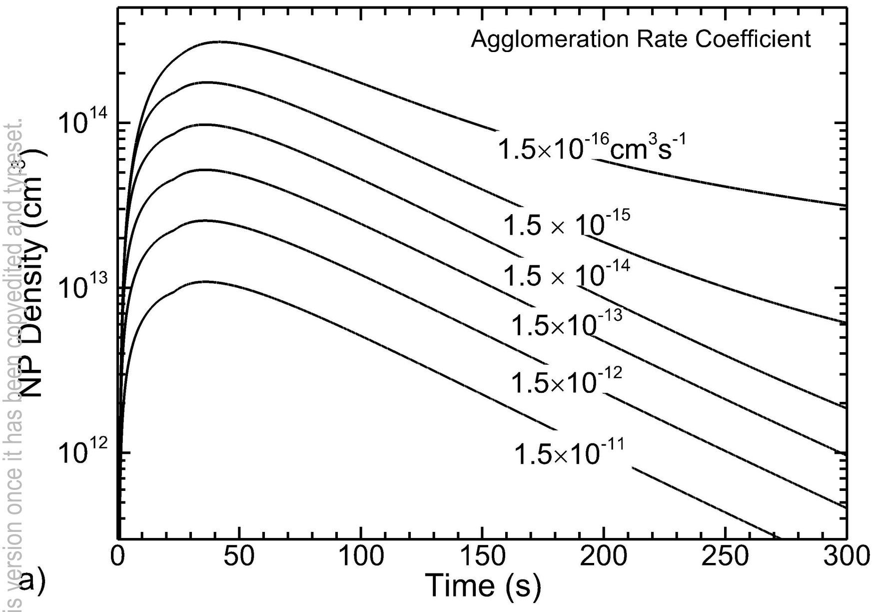
Agglomeration Rate Coefficient
1.5×10^-16 cm^3s^-1
1.5 × 10^-15
1.5 × 10^-14
1.5×10^-13
1.5×10^-12
1.5×10^-11
NP Density (cm^-3)
10^14
10^13
10^12
0
50
100
150
200
250
300
Time (s)

a)

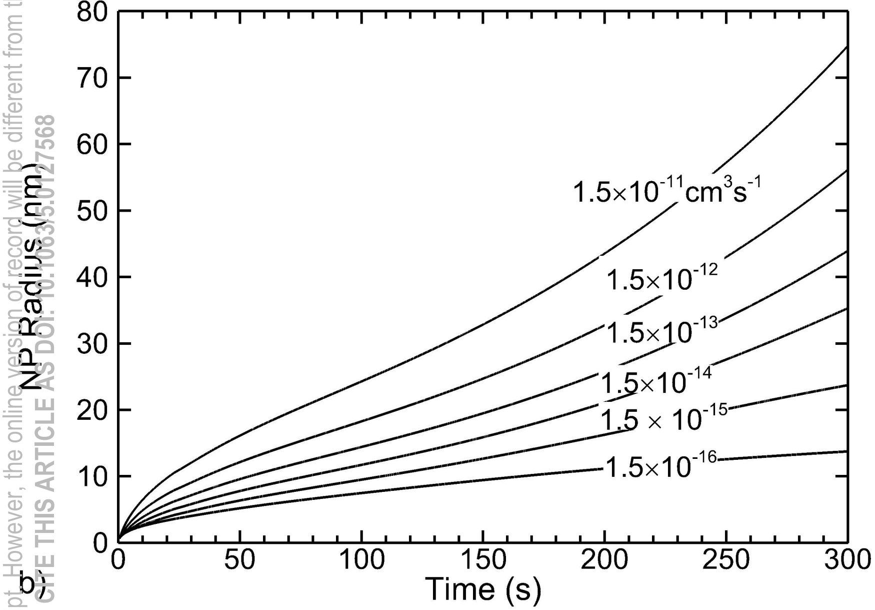
1.5×10^-11 cm^3s^-1
1.5×10^-12
1.5×10^-13
1.5×10^-14
1.5 × 10^-15
1.5×10^-16
NP Radius (nm)
0
10
20
30
40
50
60
70
80
0
50
100
150
200
250
300
Time (s)

b)

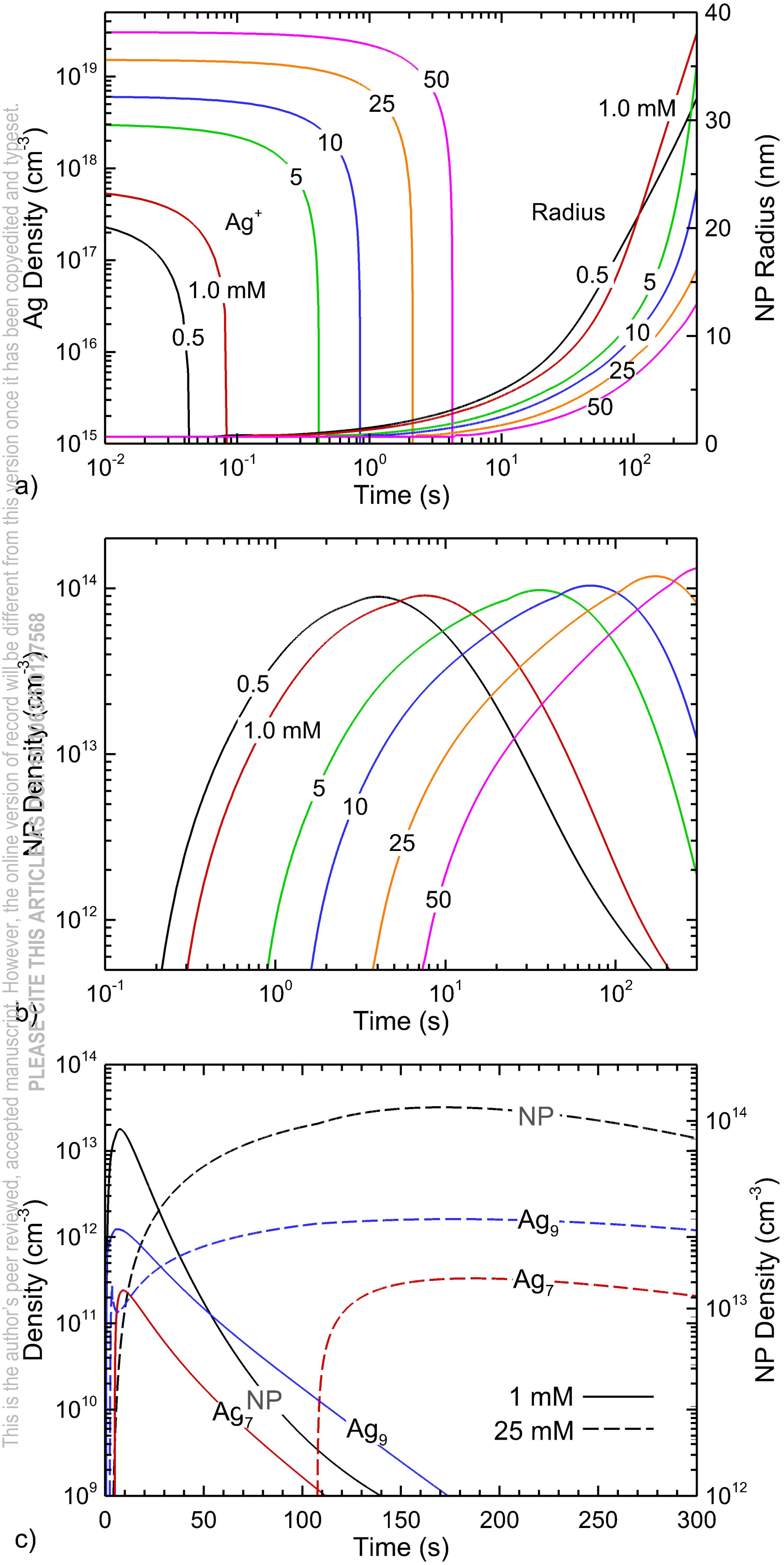
a)
Ag Density (cm^{-3})
NP Radius (nm)
Time (s)
10^{15}
10^{16}
10^{17}
10^{18}
10^{19}
10^{-2}
10^{-1}
10^{0}
10^{1}
10^{2}
0
10
20
30
40
Ag^{+}
0.5
1.0 mM
5
10
25
50
Radius
1.0 mM
0.5
5
10
25
50
b)
NP Density (cm^{-3})
Time (s)
10^{12}
10^{13}
10^{14}
10^{-1}
10^{0}
10^{1}
10^{2}
0.5
1.0 mM
5
10
25
50
c)
Density (cm^{-3})
NP Density (cm^{-3})
Time (s)
10^{9}
10^{10}
10^{11}
10^{12}
10^{13}
10^{14}
10^{12}
10^{13}
10^{14}
0
50
100
150
200
250
300
NP
Ag$_9$
Ag$_7$
Ag$_7$
NP
Ag$_9$
1 mM
25 mM

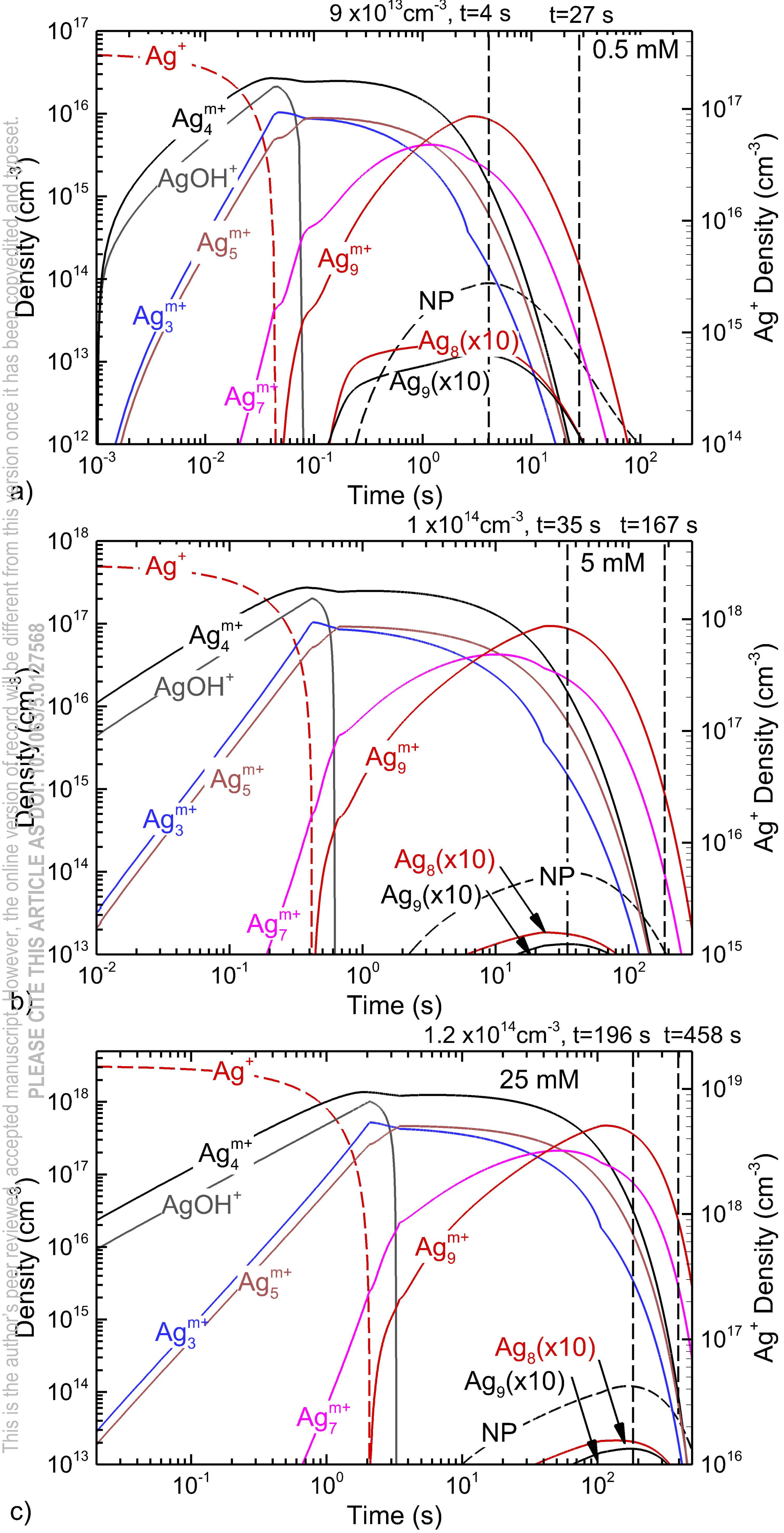
9 x10^13 cm^-3, t=4 s
t=27 s
0.5 mM
Ag^+
Ag_4^m+
AgOH^+
Ag_5^m+
Ag_3^m+
Ag_7^m+
Ag_9^m+
NP
Ag_8(x10)
Ag_9(x10)
Density (cm^-3)
Ag^+ Density (cm^-3)
Time (s)
a)
1 x10^14 cm^-3, t=35 s
t=167 s
5 mM
Ag^+
Ag_4^m+
AgOH^+
Ag_5^m+
Ag_3^m+
Ag_7^m+
Ag_9^m+
Ag_8(x10)
Ag_9(x10)
NP
Density (cm^-3)
Ag^+ Density (cm^-3)
Time (s)
b)
1.2 x10^14 cm^-3, t=196 s
t=458 s
25 mM
Ag^+
Ag_4^m+
AgOH^+
Ag_5^m+
Ag_3^m+
Ag_7^m+
Ag_9^m+
Ag_8(x10)
Ag_9(x10)
NP
Density (cm^-3)
Ag^+ Density (cm^-3)
Time (s)
c)

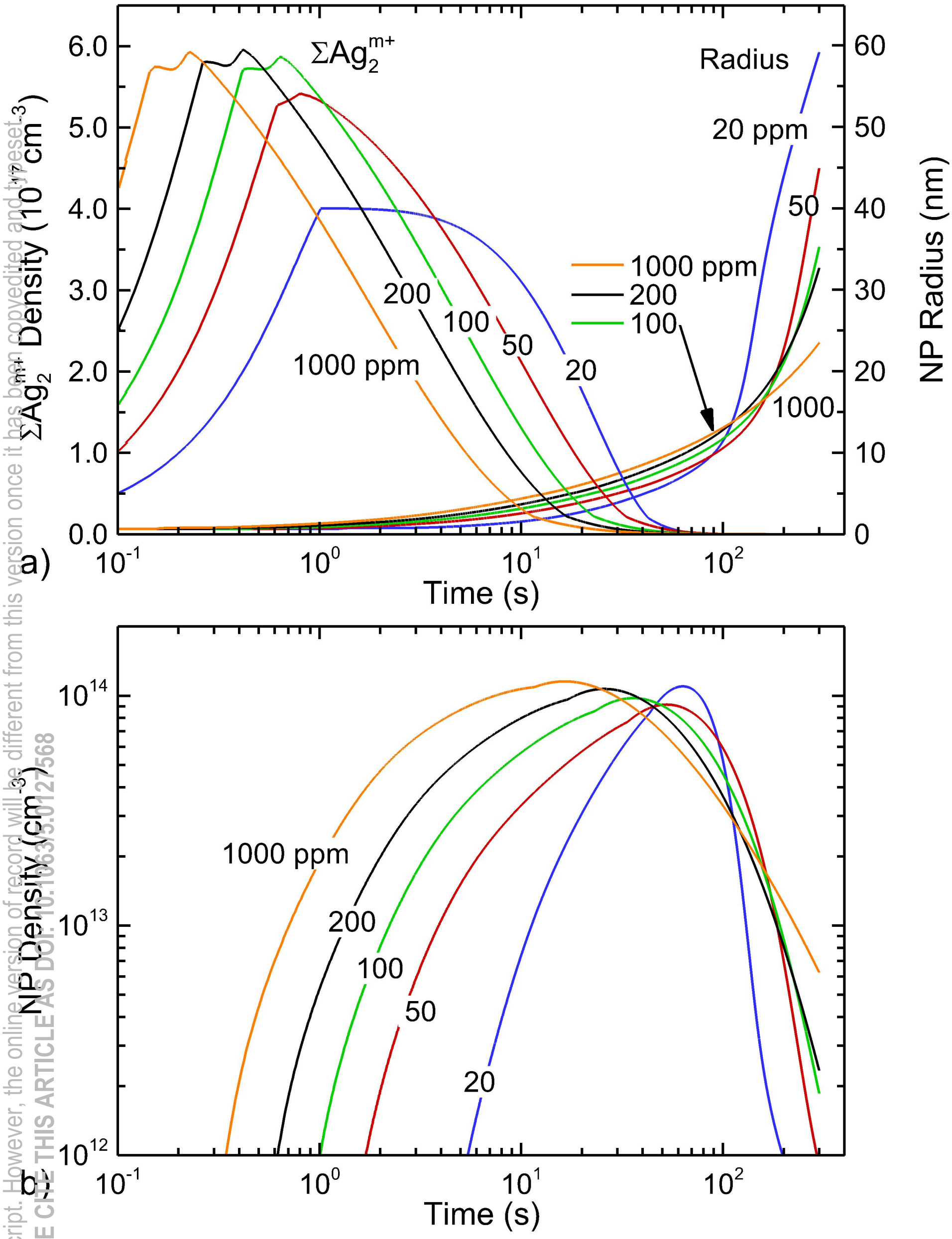
ΣAg_2^{m+}
Radius
20 ppm
50
1000 ppm
200
100
1000
200
100
50
20
1000 ppm
ΣAg_2^{m+} Density (10^{17} cm^{-3})
NP Radius (nm)
6.0
5.0
4.0
3.0
2.0
1.0
0.0
60
50
40
30
20
10
0
a)
10^{-1}
10^{0}
10^{1}
10^{2}
Time (s)
NP Density (cm^{-3})
10^{14}
10^{13}
10^{12}
1000 ppm
200
100
50
20
b)
10^{-1}
10^{0}
10^{1}
10^{2}
Time (s)

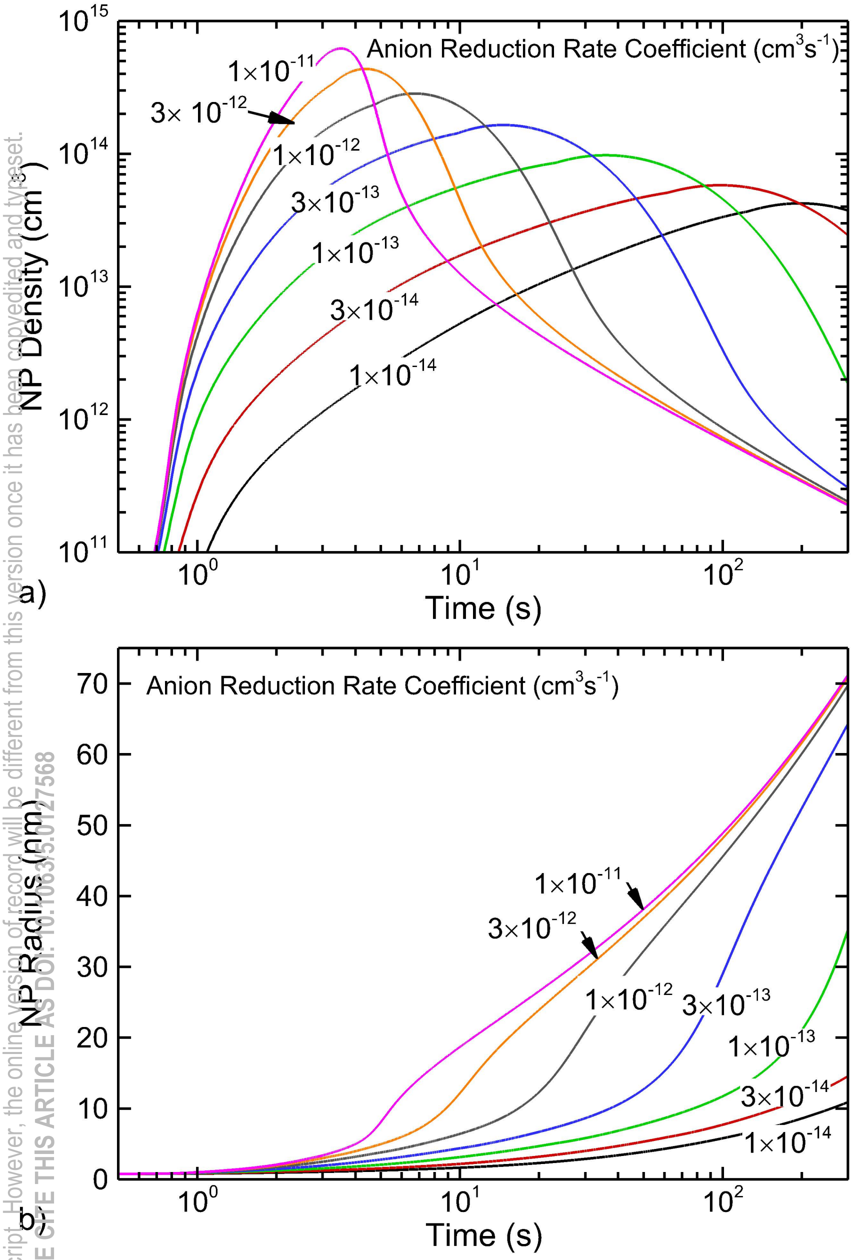
a)
NP Density (cm^{-3})
Time (s)
Anion Reduction Rate Coefficient (cm^{3}s^{-1})
1×10^{-11}
3× 10^{-12}
1×10^{-12}
3×10^{-13}
1×10^{-13}
3×10^{-14}
1×10^{-14}
10^{15}
10^{14}
10^{13}
10^{12}
10^{11}
10^{0}
10^{1}
10^{2}
b)
NP Radius (nm)
Time (s)
Anion Reduction Rate Coefficient (cm^{3}s^{-1})
1×10^{-11}
3×10^{-12}
1×10^{-12}
3×10^{-13}
1×10^{-13}
3×10^{-14}
1×10^{-14}
70
60
50
40
30
20
10
0
10^{0}
10^{1}
10^{2}

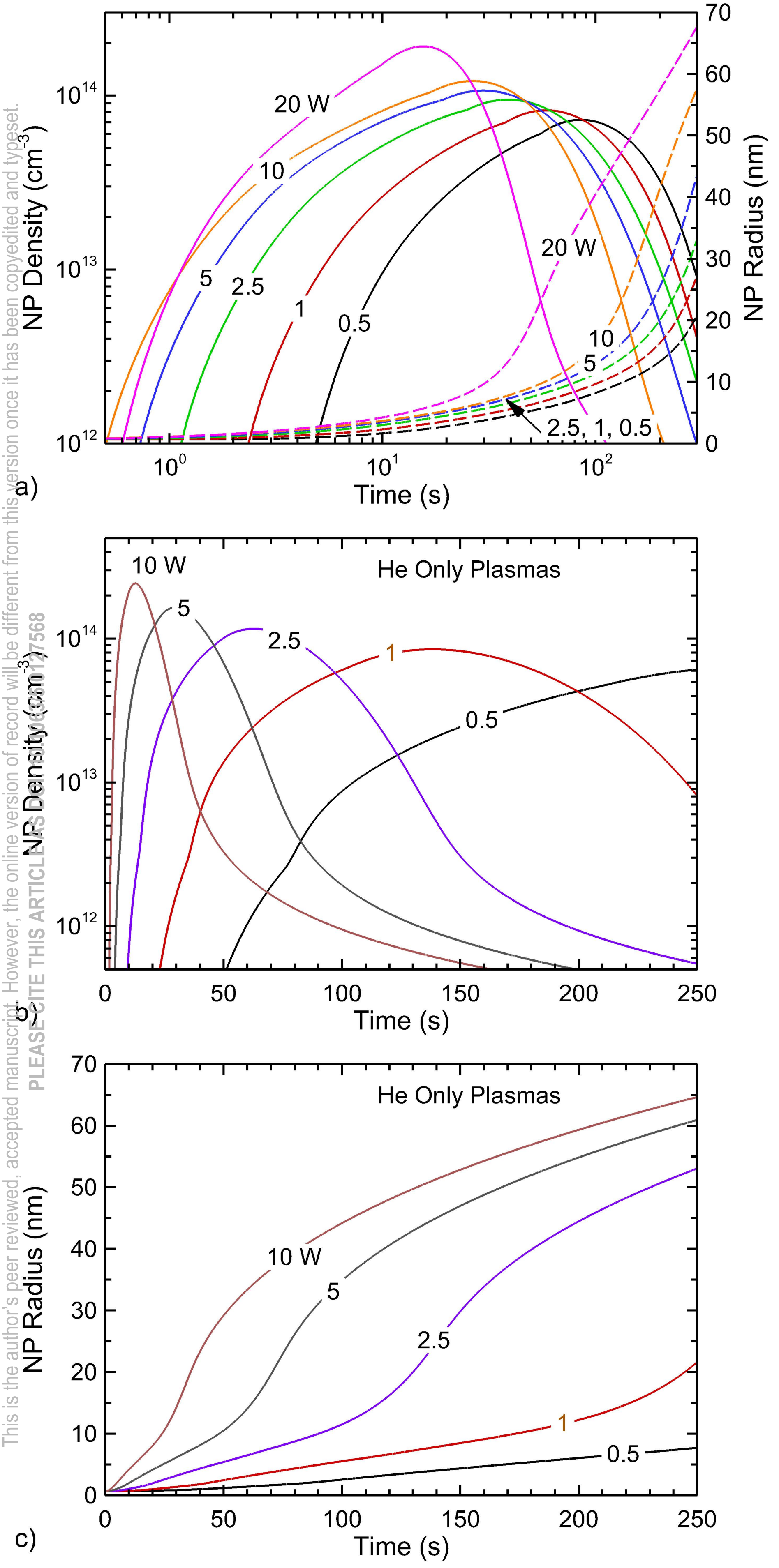
NP Density (cm^{-3})
NP Radius (nm)
Time (s)
10^{14}
10^{13}
10^{12}
10^{0}
10^{1}
10^{2}
70
60
50
40
30
20
10
0
20 W
10
5
2.5
1
0.5
20 W
10
5
2.5, 1, 0.5
a)
10 W
He Only Plasmas
5
2.5
1
0.5
NP Density (cm^{-3})
10^{14}
10^{13}
10^{12}
0
50
100
150
200
250
Time (s)
b)
He Only Plasmas
NP Radius (nm)
70
60
50
40
30
20
10
0
10 W
5
2.5
1
0.5
0
50
100
150
200
250
Time (s)
c)

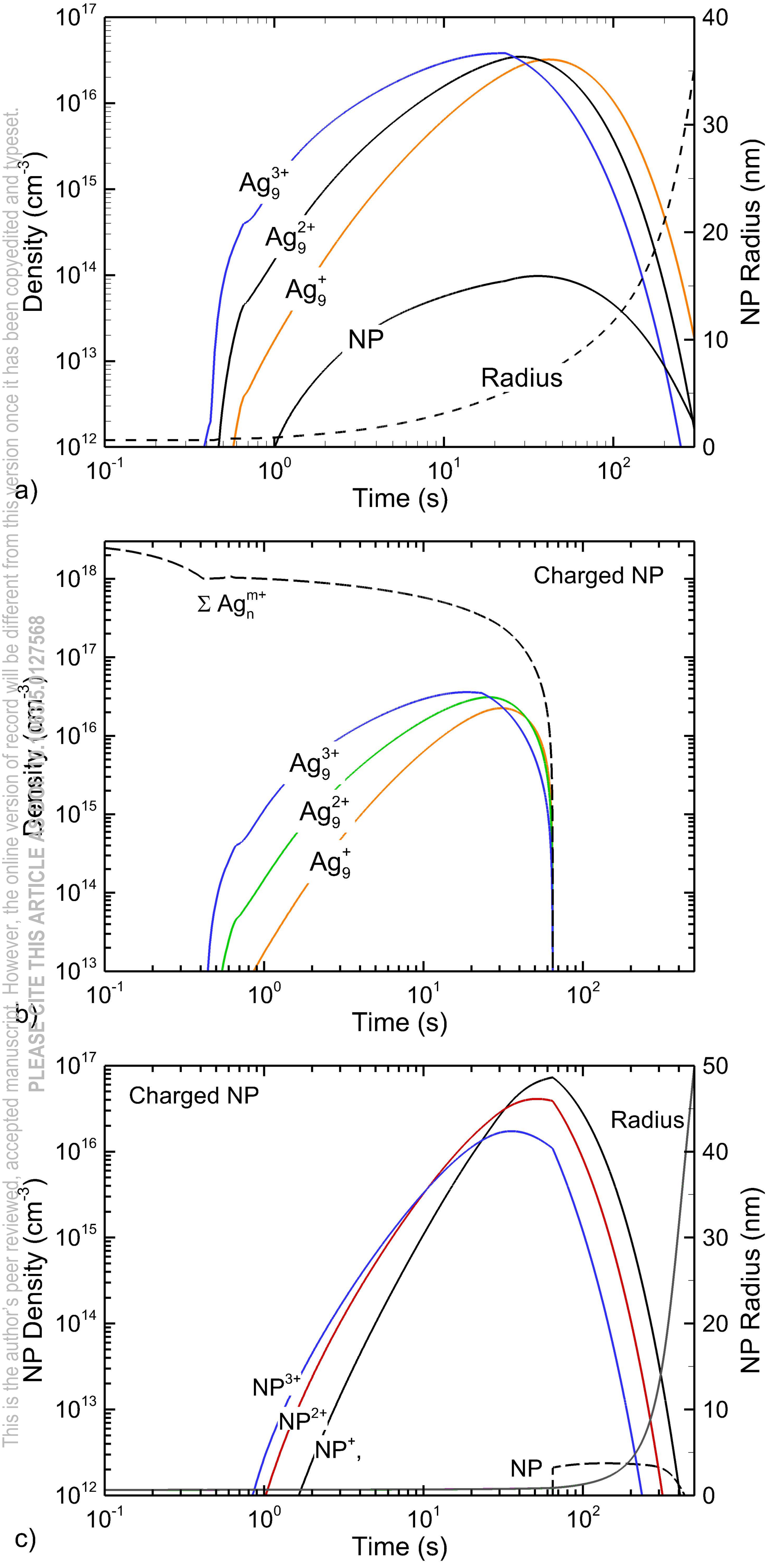
a)
Density (cm^{-3})
NP Radius (nm)
Time (s)
Ag_9^{3+}
Ag_9^{2+}
Ag_9^{+}
NP
Radius
10^{12}
10^{13}
10^{14}
10^{15}
10^{16}
10^{17}
0
10
20
30
40
10^{-1}
10^{0}
10^{1}
10^{2}
b)
Density (cm^{-3})
Time (s)
Charged NP
ΣAg_n^{m+}
Ag_9^{3+}
Ag_9^{2+}
Ag_9^{+}
10^{13}
10^{14}
10^{15}
10^{16}
10^{17}
10^{18}
10^{-1}
10^{0}
10^{1}
10^{2}
c)
NP Density (cm^{-3})
NP Radius (nm)
Time (s)
Charged NP
Radius
NP^{3+}
NP^{2+}
NP^{+},
NP
10^{12}
10^{13}
10^{14}
10^{15}
10^{16}
10^{17}
0
10
20
30
40
50
10^{-1}
10^{0}
10^{1}
10^{2}

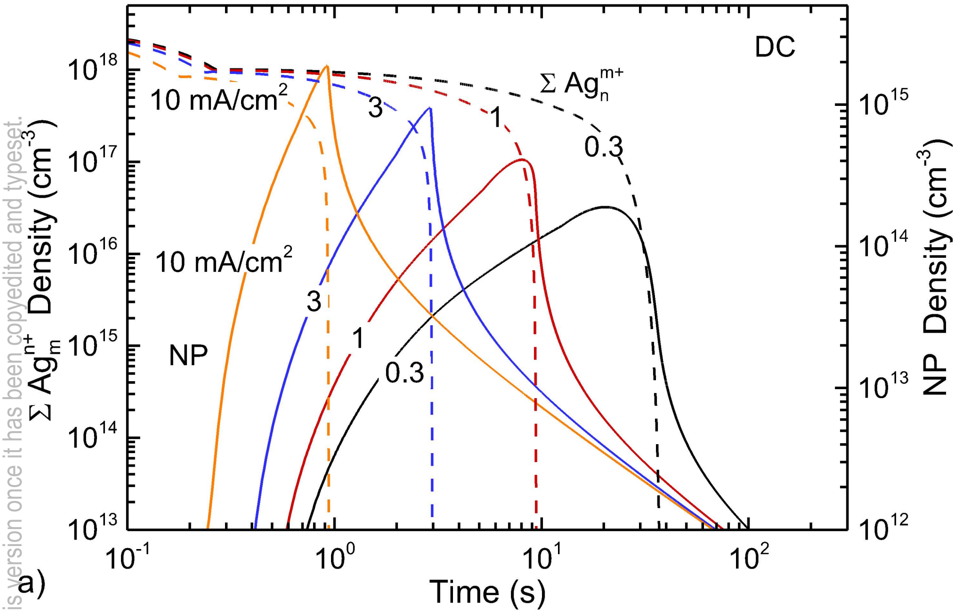
DC
Σ Ag_n^{m+}
10 mA/cm^2
3
1
0.3
10 mA/cm^2
3
1
0.3
NP
10^{13}
10^{14}
10^{15}
10^{16}
10^{17}
10^{18}
Σ Ag_m^{n+} Density (cm^{-3})
10^{12}
10^{13}
10^{14}
10^{15}
NP Density (cm^{-3})
10^{-1}
10^{0}
10^{1}
10^{2}
Time (s)
a)

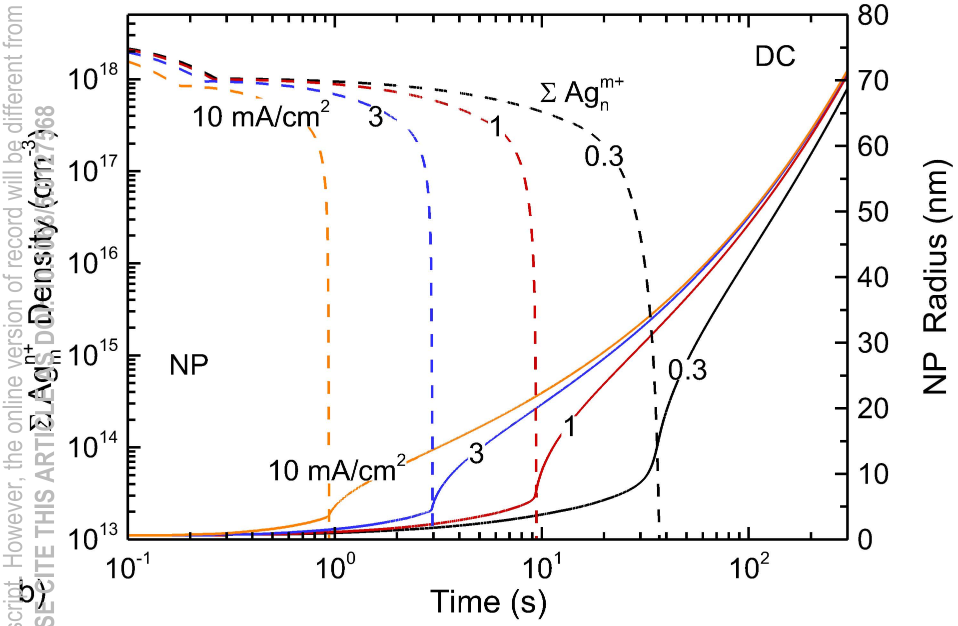
DC
Σ Ag_n^{m+}
10 mA/cm^2
3
1
0.3
10 mA/cm^2
3
1
0.3
NP
10^{13}
10^{14}
10^{15}
10^{16}
10^{17}
10^{18}
Σ Ag_m^{n+} Density (cm^{-3})
0
10
20
30
40
50
60
70
80
NP Radius (nm)
10^{-1}
10^{0}
10^{1}
10^{2}
Time (s)
b)